Monthly Notices of the ROYAL ASTRONOMICAL SOCIETY

MNRAS **512,** 2537–2555 (2022) https://doi.org/10.1093/mnras/stac629
Advance Access publication 2022 March 24

High and low Sérsic index bulges in Milky Way- and M31-like galaxies: origin and connection to the bar with TNG50

Ignacio D. Gargiulo [1,2★] Antonela Monachesi [3,4] Facundo A. Gómez [3,4] Dylan Nelson [5] Annalisa Pillepich [6] Rüdiger Pakmor [7] R. J. J. Grand [7,8,9] Francesca Fragkoudi,[10] Lars Hernquist,[11] Mark Lovell[12] and Federico Marinacci [13]

[1]*Instituto de Astrofísica de La Plata (CCT La Plata, CONICET, UNLP), Observatorio Astronómico, Paseo del Bosque B1900FWA, La Plata, Argentina*
[2]*Consejo Nacional de Investigaciones Científicas y Técnicas (CONICET), Rivadavia 1917, Buenos Aires, Argentina*
[3]*Instituto de Investigación Multidisciplinar en Ciencia y Tecnología, Universidad de La Serena, Raúl Bitrán 1305, La Serena, Chile*
[4]*Departamento de Astronomía, Universidad de La Serena, Av. Juan Cisternas 1200 Norte, La Serena, Chile*
[5]*Institut für Theoretische Astrophysik, Zentrum für Astronomie, Universität Heidelberg, Albert-Ueberle-Str. 2, D-69120 Heidelberg, Germany*
[6]*Max-Planck-Institut für Astronomie, Königstuhl 17, D-69117 Heidelberg, Germany*
[7]*Max-Planck-Institut für Astrophysik, Karl-Schwarzschild-Str. 1, D-85748 Garching, Germany*
[8]*Instituto de Astrofísica de Canarias, Calle Váa Láctea s/n, E-38205 La Laguna, Tenerife, Spain*
[9]*Departamento de Astrofísica, Universidad de La Laguna, Av. del Astrofísico Francisco Sánchez s/n, E-38206 La Laguna, Tenerife, Spain*
[10]*European Southern Observatory, Karl-Schwarzschild-Str 2, D-85748 Garching-bei-München, Germany*
[11]*Institute for Theory and Computation, Harvard-Smithsonian Center for Astrophysics, 60 Garden St, MS-51, Cambridge, MA 02138, USA*
[12]*Center for Astrophysics and Cosmology, Science Institute, University of Iceland, Dunhaga 5, 107 Reykjavák, Iceland*
[13]*Department of Physics and Astronomy 'Augusto Righi', Università di Bologna, Via Gobetti 93/2, I-40129 Bologna, Italy*

Accepted 2022 March 2. Received 2022 February 16; in original form 2021 November 17

ABSTRACT

We study bulge formation in MW/M31-like galaxies in a Λ-cold dark matter scenario, focusing on the origin of high- and low-Sersic index bulges. For this purpose, we use TNG50, a simulation of the IllustrisTNG project that combines a resolution of $\sim 8 \times 10^4$ $M_\odot$ in stellar particles with a cosmological volume 52 cMpc in extent. We parametrize bulge surface brightness profiles by the Sérsic index and the bulge-to-total (B/T) ratio obtained from two-component photometric decompositions. In our sample of 287 MW/M31-like simulated galaxies, 17.1 per cent of photometric bulges exhibit high-Sérsic indices and 82.9 per cent show low-Sérsic indices. We study the impact that the environment, mergers and bars have in shaping the surface brightness profiles. We find no correlation between bulge properties and the environment where they reside. Simulated galaxies with higher Sérsic indices show, on average, a higher fraction of *ex situ* stars in their kinematically selected bulges. For this bulge population, the last significant merger (total mass ratio $m_{\rm sat}/m_{\rm host} > 0.1$) occurs, on average, at later times. However, a substantial fraction of low-Sérsic index bulges also experience a late significant merger. We find that bars play an important role in the development of the different types of photometric bulges. The fraction of simulated galaxies with bars is smaller for the high- than for the low-Sérsic index population, reaching differences of 20 per cent at $z > 1$. Simulated galaxies with high fractions of *ex situ* stars in the bulge do not develop strong bars. Conversely, simulated galaxies with long-lived strong bars have bulges with *ex situ* fractions, $f_{ex\ situ} < 0.2$.

Key words: galaxies: bar – galaxies: bulges – methods: numerical.

1 INTRODUCTION

The galactic bulge has been, arguably, the least studied galactic component with cosmological simulations evolved within the current Λ-cold dark matter paradigm (ΛCDM, see Peebles 2020a, and references therein). One of the main historical reasons behind this was the lack of computational resources needed to resolve the interaction of the many particles that co-exist within the volume of the galactic central region. Additionally, bulges are not easy to define and, as a result, theoretical works have been focused on the study of central spheroidal regions (e.g. Tissera et al. 2018; Tacchella et al. 2019). The 'photometric bulge' is, perhaps, a less ambiguous definition of a bulge (see Gadotti 2012, for a succinct overview on bulge definitions). This observational definition refers to the excess of starlight in the central regions of a disc galaxy with respect to the exponential profile that is used to represent the surface brightness of the disc component. Indeed, it is a common practice to photometrically decompose the surface brightness profile of a disc galaxy by fitting two smooth functional components (Freeman 1970; Kent 1985; Andredakis, Peletier & Balcells 1995). An exponential profile represents the disc and a Sérsic profile (Sérsic 1963) accounts for the central part of the galaxy. The Sérsic function includes a free parameter, known as the Sérsic index, that modulates the shape of the Sérsic profile. A Sérsic index $n = 1$ results in an exponential profile, while $n = 4$ is equivalent to the de Vaucouleurs profile (de

★ E-mail: ignacio.gargiulo@gmail.com

Vaucouleurs 1948), that is generally used to fit the surface brightness profiles of elliptical galaxies. A larger Sérsic index value is indicative of a more concentrated light profile (see Graham & Driver 2005, for a complete reference of the related mathematical expressions).

The photometric bulge definition has two main advantages. First, it is independent of the galaxy inclination (under the assumption of no dust), meaning that one can consistently compare large samples of observed photometric bulges, irrespective of galaxy orientation. Secondly, it is objective and reproducible. However, this lack of ambiguity comes with the price of an excess of vagueness. This definition of a photometric bulge in a single galaxy includes in this component all the light of the stars that are not part of the disc, which can be of very different origins. Moreover, the photometric-based definition is also prone to put in one single category stellar components with markedly different kinematics (Du et al. 2020, 2021).

It is worth noting that fitting procedures that include more than two components, like bars, rings, or nuclear clusters, when present, are also common (e.g. Laurikainen, Salo & Buta 2005; Weinzirl et al. 2009). However, when only two components are fitted to 1D surface brightness distributions of a sample of disc galaxies in the local Universe, an interesting trend is found. Using high-resolution images from *HST* in the *V* band (Fisher & Drory 2008) and *Spitzer* images in near-infrared (Fisher & Drory 2010), it was shown that the Sérsic index distribution obtained from the two-component photometric decompositions shows a correlation with bulge morphological type. Bulges morphologically classified as pseudo-bulges, those with *morphology reminiscent of disc galaxies, with inner spiral structure, rings, or bars*, infrequently show $n > 2$. On the other hand, those classified as classical bulges, *easily recognized as having morphologies very similar to E-type galaxies*, rarely show a Sérsic index $n < 2$. For a complete and updated guide of bulge classification into classical and pseudo-bulges according to these authors we refer the reader to Fisher & Drory (2016).

Although classification into these two distinct types of bulges is not always straightforward because of the existence of overlapping criteria in composite systems (e.g. Méndez-Abreu et al. 2014; Erwin et al. 2015), there are clear indications of the existence of more than one photometric bulge formation channel, underlying the differences observed in the bulge surface brightness profiles. The physical origin of this apparent dichotomy is not well understood.

It should be noted that classification into classical and pseudo-bulges is also carried out using 2D surface brightness image decomposition of galaxies and invoking other criteria. For example Gadotti (2009) classifies bulges according the position of galaxies in the mean surface brightness – effective radius ($<\mu_e> - r_{\rm eff}$) diagram known as the Kormendy relation (Kormendy 1977) and Luo et al. (2020) use the $\Delta\Sigma_1$ parameter, that measures the relative central stellar-mass surface density within the inner kpc of galaxies. Although the same terminology of pseudo- and classical bulge is used in these lines of work, the classification criteria differ from those of Fisher & Drory (2016) and the dichotomy with bulge-type and Sérsic index does not arise with clarity.

Galaxies of the mass of our Galaxy, the Milky Way (MW) and our neighbour Andromeda (M31), are particularly interesting targets for studying the origin of different types of photometric bulges. The bulge of the MW seems to be a prototypical case formed exclusively via secular evolution (see e.g. Shen et al. 2010; Fragkoudi et al. 2020), except for a small fraction of stars (Kunder et al. 2016, 2020). M31, for its part, shows a more massive bulge (Saglia et al. 2010) with a classical or composite bulge morphology (Mould 2013; Blaña Díaz et al. 2017, 2018). Beyond the Local Group, MW/M31-sized galaxies in the nearby Universe show a great diversity in their bulge properties (Bell et al. 2017). A successful model of galaxy formation within the ΛCDM paradigm should be able to describe this observed diversity.

From a theoretical perspective, galaxy formation models establish that two broad main drivers of photometric bulge formation are mergers (Toomre 1977; Hopkins et al. 2009; Brooks & Christensen 2016) and secular evolution (see e.g. Kormendy & Kennicutt 2004; Athanassoula 2005). A third proposed channel of bulge formation is the infall of giant clumps of de-stabilized gas into the central regions of the galaxy, due to dynamical friction, in the early epochs of galaxy formation (Elmegreen 1995; Dekel, Sari & Ceverino 2009; Elmegreen et al. 2009; Ceverino, Dekel & Bournaud 2010). Historically, most theoretical works on bulge formation have focused on isolated simulations or tailored interactions with constrained orbital parameters. These have the advantage of being adequate to study in detail the effects of a given formation mechanism at the expense of losing perspective on the complex interactions and feedback loops between different physical processes. The study of bulge formation within a cosmological framework was done almost exclusively in the zoom-in regime, where a single DM halo is selected and the galaxy within it can be re-simulated at a higher resolution (Guedes et al. 2013; Okamoto 2013; Buck et al. 2018; Tissera et al. 2018; Gargiulo et al. 2019). The main disadvantage is the limited number of the available simulated galaxies. Recently, for example, Gargiulo et al. (2019) studied the photometric bulges of a sample of 30 high-resolution simulations from the Auriga project (Grand et al. 2017) and found that all of them showed low Sérsic indices and most of them had properties more akin to pseudo-bulges. They suggested that the galaxy sample may have an environmental bias due to the isolation criterion used to select the DM haloes in the parent simulation, where galaxies were later re-simulated.

The advent of joint efforts to run cosmological simulations in large volumes, with particle and dynamical resolution proper of the re-simulation regime, such as the TNG50 simulation of the IllustrisTNG project (Nelson et al. 2019b; Pillepich et al. 2019) as well as recent projects such as New-Horizon (Dubois et al. 2020), represents a renewed opportunity to study in detail the subject of bulge formation, as done recently, for example, by Du et al. (2021). It is now possible to explore the complexity associated to the evolution in a cosmological context in a large sample of galaxies that is exempt of an environmental selection bias.

In this work, we will make use of the TNG50 simulation (Pillepich et al. 2019; Nelson et al. 2019a, TNG50 from now on), the cosmological box with highest resolution of the three IllustrisTNG volumes. We study the properties of photometric bulges in a sample of MW/M31-like galaxies and search for the drivers of their formation. We will focus on the origin of the different bulge surface brightness profiles of MW/M31-like galaxies, characterized by the Sérsic index and bulge-to-total ratio. We place emphasis on the effects of the environment, the role of mergers, and the influence of bars.

This paper is organized as follows. In Section 2, we describe the methods and simulation used throughout this work, and define our sample of MW-like galaxies selected from the cosmological box. In Section 3.1, we explore the influence of environment on the type of photometric bulge in our sample of simulated galaxies. In Section 4, we characterize the populations of stars born *in situ* and those accreted in mergers (*ex situ*) that populate the bulges at $z = 0$. In Section 5, we explore the role of mergers in shaping the surface brightness profile in the simulated galaxies. In Section 6, we study the impact of bars in the formation of photometric bulges. In Section 7, we discuss our results in a broader context and finally, in Section 8, we summarize our results and present our conclusions.

Table 1. Attributes of the simulation analysed in this work. The properties shown in rows are: box side-length (co-moving units); number of initial gas cells and dark matter particles; mean baryon and dark matter particle mass resolution (solar masses); mean size of star-forming gas cells. For a complete description of the simulation see the IllustrisTNG project homepage.

Run		**TNG50-1**
$L_{\rm box}$	(Mpc)	51.7^3
$N_{\rm DM,GAS}$	–	2160^3
$m_{\rm baryon}$	($M_\odot$)	8.5×10^4
$m_{\rm DM}$	($M_\odot$)	4.6×10^5
$<r_{\rm gas,SF}>$	(pc)	∼100–150
$\epsilon_{\rm DM,\star}$	(pc)	290

2 METHODS

In this section, we describe the simulation used throughout this work and the selection of the sample of simulated MW/M31-like galaxies. We characterize the two different methods to quantify the local density for each galaxy in our sample. We also present the methodology used to measure the bar strengths in simulated galaxies.

2.1 Simulation

The Illustris-*The Next Generation* project (hereafter IllustrisTNG, Marinacci et al. 2018; Naiman et al. 2018; Nelson et al. 2018; Springel et al. 2018; Pillepich et al. 2018b) is a collection of cosmological magnetohydrodynamical simulations that comprise a set of cosmological boxes with different sizes and mass resolutions,[1] and were carried-out with the magneto-hydrodynamical moving-mesh code AREPO (Springel 2010). Currently, all simulations, including TNG50, are publicly available (Nelson et al. 2019a).

IllustrisTNG is the successor of the original Illustris project (Genel et al. 2014; Vogelsberger et al. 2014a, b; Nelson et al. 2015) and is based on a substantially updated physical model (Weinberger et al. 2017; Pillepich et al. 2018b). One of the main distinct aspects of the IllustrisTNG physical model with respect to the one used in Illustris is the treatment of the energetic feedback from supermassive black holes (BHs). In particular, the low accretion regime of BH feedback (also known as 'radio mode', Croton et al. 2006) was strongly modified. The bubble radio feedback based on the model from Sijacki et al. (2007) was replaced by small-scale, kinetic winds (Weinberger et al. 2017). Other important features are the inclusion of seed magnetic fields that evolve and are amplified during cosmic evolution (Pakmor, Marinacci & Springel 2014) and a more efficient numerical implementation in AREPO. Altogether, the updated IllustrisTNG physical model helps to reduce discrepancies with observational constraints identified for the original Illustris simulations (Nelson et al. 2015, Section 6). A detailed analysis of the updated physical scheme used in IllustrisTNG and its impact on the galaxy population can be found in Pillepich et al. (2018a).

In this work, we make use of the highest resolution version of IllustrisTNG, the TNG50-1 run (hereafter TNG50, Pillepich et al. 2019; Nelson et al. 2019b). The main parameters of the TNG50 simulations are shown in Table 1. The TNG50-1 simulation consists of a periodic volume of $L_{\rm box} = 35\,h^{-1} \sim 50$ cMpc in extent with a gas cell mass resolution of 8.5×10^4 $M_\odot$. This resolution is only a factor of approximately two worse than that of the Auriga simulations (Grand et al. 2017, hereafter G2017) in their level 4 resolution hierarchy. Thus, TNG50 allows us to study the inner structure of a large sample of MW/M31-like galaxies (see next section), evolving under the influence of the cosmological environment, with a numerical resolution close to those obtained in typical zoom-in re-simulations.

[1] https://www.tng-project.org

2.2 Sample of MW/M31-like galaxies

We select our sample of MW/M31-like galaxies in TNG50 based on the procedure described in Pillepich et al. (in preparation, P22 from now on) and used in Engler et al. (2021) and Pillepich et al. (2021). Note however that in this work we relaxed their isolation criterion to properly account for possible environmental effects. We select MW/M31 analogs such that:

(i) They have stellar masses $M_\star$ in the range $[10^{10.5}$–$10^{11.2}]M_\odot$, where $M_\star$ is the sum of all stellar particles enclosed in a sphere of 30 kpc, centered at the most bound DM particle, at $z = 0$.

(ii) They have a disc morphology. To quantify this, we select galaxies with $s < 0.45$, where $s = c/a$ is the minor-to-major axial ratio of the stellar moment of inertia tensor, measured between one and two times the stellar half-mass radius. Additionally, 25 galaxies with $s > 0.45$ in the adopted mass range that show a clear disc morphology by visually inspecting synthetic 3-band stellar-light images are added to the simulated galaxy sample.

A total of 287 MW-like galaxies following these criteria are found in TNG50. As stated above, in P22 a third criterion based on isolation is applied to this sample of galaxies: no other galaxy with stellar mass $M_\star > 10.5$ should lie within a distance of 500 kpc of the corresponding simulated galaxy and the galaxy should have a host DM halo with $M_{200c} < 10^{13}\,M_\odot$, where M_{200c} is the sum of the mass of DM particles inside a sphere centred in the halo (identified with a Friend-of-Friends algorithm) within which the mean density is 200 times the critical density of the Universe. When the isolation criterion is relaxed, 89 galaxies are added to their sample of 198 simulated galaxies, summing up to the 287 galaxies of our sample.

2.2.1 Two-component decomposition of galaxies: photometric bulges

We perform a two-component decomposition of the surface brightness profiles (SBP) of the galaxies in our sample. We assume a smooth surface brightness distribution described by the sum of an exponential profile and a Sérsic (1968) function

$$I(r) = I_{\rm e,b} \exp\left\{ -b_{\rm n}\left[(r/r_{\rm eff})^{1/n} - 1\right]\right\} + I_{0,d} \exp\left[-(r/R_{\rm scale})\right], \quad (1)$$

where $r_{\rm eff}$ is the effective radius of the Sérsic model, n is the Sérsic index, $I_{\rm e,b}$ is the intensity of the bulge component at $r_{\rm eff}$, $R_{\rm scale}$ is the disc scale length and $I_{0,\rm d}$ is the central intensity of the disc component. The factor $b_{\rm n}$ is such that $\Gamma(2n) = 2\gamma(2n, b_{\rm n})$, where Γ is the complete gamma function and γ is the incomplete gamma function.

We follow Gargiulo et al. (2019, G19 hereafter) and measure the SBP from the face-on projection of each galaxy. The SBP is computed after averaging the total luminosity in the V band inside 500 pc wide concentric annuli, from just outside the resolution limit and out to the optical radius of each galaxy. Luminosities are derived from the magnitudes of the stellar particles, which are treated as single stellar populations after formation using population synthesis models (Bruzual & Charlot 2003). The resolution limit is defined as three times the minimum allowed softening length for gas cells ($3 \times \epsilon_{\rm gas,min} = 222$ pc). The optical radius is defined as the radius at which the surface brightness in the B band drops below $\mu_B = 25$ mag arcsec^{-2}.

We have to bear in mind that a relatively large fraction of the simulated galaxies of our sample contain bars at $z = 0$ (from $\sim$ 40 to $\sim$ 60 per cent, depending on the bar strength threshold used, see Section 6). We do not fit an extra component to the surface brightness profiles to account for this component, but we attempt to remove this component from the fit by masking the points that show evidence for an excess of light with respect to the disc due to a bar, spiral arm or other type of perturbations from the fit when it is identifiable in the SBP. However, contamination from the bar will be present in each of the components of the fit. If the bar is short and with low ellipticity, the majority of the bar light will be absorbed by the Sérsic fit component. In the case of long bars, the majority of their light will be part of the disc exponential profile. We deliberately choose to fit only two-component models to the SBPs. This is because the two-peaked distribution of Sérsic indices reported by Fisher & Drory (2008, 2010, 2011), was derived using two-component photometric decompositions of SBPs of galaxies. However, adding a third or more components to the SBPs would also yield interesting and complementary insights of the physical origin of photometric bulges (see e.g. Blázquez-Calero et al. 2020) and we defer this to a future work.

2.2.2 *Kinematic bulges*

To define the kinematic bulge, we select particles inside a spherical region of $2 \times r_{\rm eff}$ with circularities $|\epsilon| < 0.7$, where the circularity $|\epsilon|$ is defined as $\epsilon = J_z/J(E)$ (Abadi et al. 2003). Here, J_z is the angular momentum component perpendicular to the disc plane of a stellar particle with orbital energy E, and $J(E)$ is the maximum possible angular momentum for the given E. Particles with circularities $|\epsilon| > 0.7$ are considered disc particles. As discussed by Peebles (2020b), this particular circularity cut can include in the disc component a fraction of particles with orbits that significantly depart from circular. We note that this circularity cut is commonly assumed in the literature and, thus, it facilitates comparison with previous works. More stringent circularity cuts (e.g. $|\epsilon| > 0.8$) modify only slightly the *in situ*/*ex situ* particle fractions and our conclusions remain unmodified. The fixed spatial cut of $2 \times r_{\rm eff}$ is, in general, close to the radius beyond which the exponential disc starts to dominate the light profile. We keep this fixed definition to compare with results presented in G19 for the Auriga simulations.

2.2.3 *Environment definitions*

Our first estimate of the local density of the environment is the overdensity parameter:

$$1 + \delta = \frac{P}{P_{\rm median}}, \tag{2}$$

where P is the volumetric density of galaxies at the position of the ith MW/M31-like galaxy defined as

$$P(\mathbf{r}_{\rm i}) = \frac{3{\rm k}}{4\pi \sum_{\rm j=1}^{\rm k} {\rm d}_{\rm ij}^3}. \tag{3}$$

Here, $\mathbf{r}_{\rm i}$ is the position of the ith MW/M31-like galaxy, $\rm d_{ij}$ is the distance between the ith MW/M31-like galaxy and its jth neighbour with a mass above given mass cut, and k is the number of neighbours considered. $P_{\rm median}$ is the median volumetric density of galaxies with the adopted mass cut in the cosmological volume of the simulation.

A second approach to measure the local density of galaxies is to count neighbours in a fixed size region (e.g. Blanton & Moustakas 2009). We define a 738.2 kpc sphere around each MW/M31-like galaxy in our sample and count the number of neighbouring galaxies inside the sphere with total mass above a given mass cut.

2.2.4 *Bar strength measurement*

We compute the bar strength for galaxies in our sample by means of Fourier mode analysis (e.g. Grand et al. 2016). We define equally spaced radial annuli in the face-on projections of the disc galaxies and compute the complex Fourier coefficients to quantify azimuthal patterns in the mass distribution with n-fold axisymmetry:

$$a_n(R_j) = \sum_{i=1}^{N_R} m_i \cos(n\,\theta_i), \tag{4}$$

and

$$b_n(R_j) = \sum_{i=1}^{N_R} m_i \sin(n\,\theta_i), \tag{5}$$

where a_n and b_n are the real and imaginary components of the Fourier coefficients. The sum is over the ith particle in the jth annulus. Here, m_i and θ_i are the mass and azimuthal angle of the ith particle, respectively. We characterize the strength of the nth Fourier mode by its amplitude, given by

$$B_n(R_j, t) = \sqrt{a_n(R_j, t)^2 + b_n(R_j, t)^2}. \tag{6}$$

The second mode, $n = 2$, corresponds to a bisymmetric signal with a periodicity of π radians, such as a double arm or a bar. In order to correctly quantify the bar strength one should determine where the bar ends and the spiral arms begin. To do so, we make use of the bar phase angle, which is computed as:

$$\theta_2' = \frac{1}{2}{\rm atan2}(b_2, a_2). \tag{7}$$

The bar phase angle remains almost constant in consecutive radial annuli until the bar ends. Following Grand et al. (2016) we define the bar length, i.e. the bar semimajor axis, as the radius at which the difference in the phase angle between two consecutive radial bins is larger than 0.5. Finally, the mass-weighted mean of the amplitude of the $n = 2$ Fourier mode within the bar region, i.e. the bar strength, is defined as:

$$A_2(t) = \frac{\sum_j B_2(R_j, t)}{\sum_j B_0(R_j, t)}. \tag{8}$$

We note that another usual definition for the bar strength is to consider the maximum value of the normalized amplitude of the $n = 2$ Fourier mode, instead of the weighted mean average of the amplitude inside the bar region (see e.g. Athanassoula, Machado & Rodionov 2013). We computed the bar strength following this definition and compared the results obtained with both approaches. When using the maximum normalized amplitude as proxy for the bar strength, the nominal values obtained are larger on average. If the bar strength threshold to consider a galaxy as strongly barred is selected accordingly, the results look qualitatively the same and the conclusions of this paper remain unchanged.

3 THE BULGES OF TNG50 MW/M31-LIKE GALAXIES

We begin by analysing the general properties of our sample of 287 MW/M31-like simulated galaxies. Fig. 1 shows a selection of 9

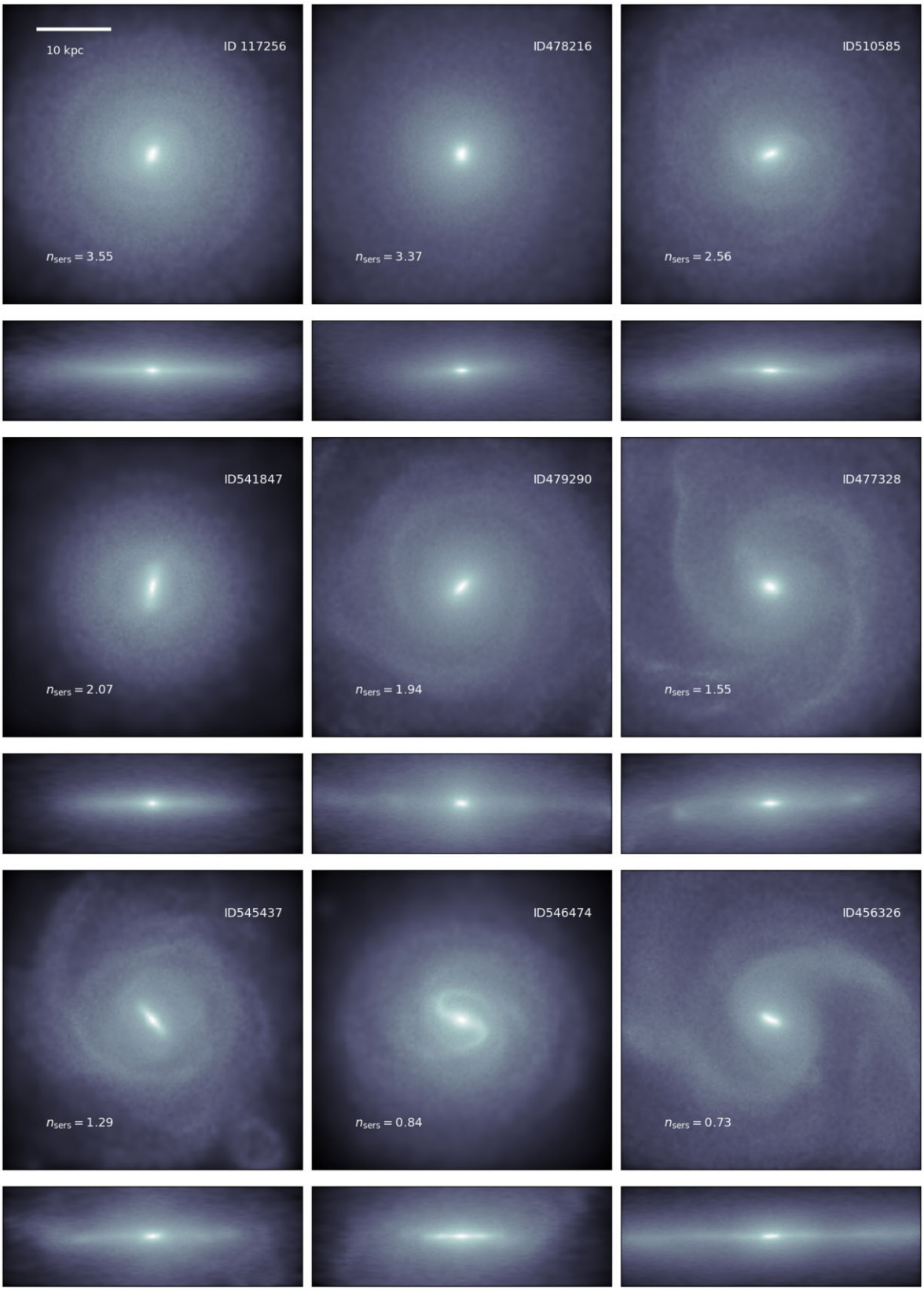

Figure 1. Face-on and edge-on projections of mock images based on the stellar density of nine examples of simulated galaxies from the sample used in this work, composed of 287 TNG50 MW/M31-like galaxies at $z = 0$. Galaxies are ordered from the top left corner to the right bottom corner by the Sérsic index of the photometric bulge component. In each panel, the identifier of the galaxy in the simulation is shown in the top right corner, and the Sérsic index in the bottom left corner. A scale of 10 kpc is indicated by the white bar in the top left panel. Galaxies with higher Sérsic bulges show featureless discs, and those with lower Sérsic are prone to exhibit spiral arms and stronger features.

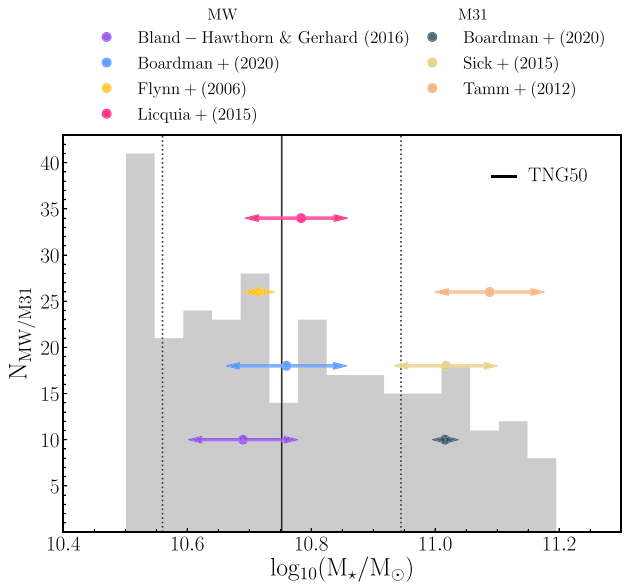

Figure 2. Stellar mass distribution of the sample of 287 TNG50 MW/M31-like galaxies described in Section 2.2. The solid black line indicates the median of the distribution and the dotted black lines show the interquartile range. The coloured circles with bidirectional arrows indicate the estimated ranges for the MW and M31 stellar mass, from different authors as indicated in the legend and cited in the text.

galaxies from our sample at $z = 0$, ordered by their Sérsic index (see Section 2.2.1) from left to right and top to bottom. These examples highlight the differences of the concentrated central regions and featureless discs of galaxies with high Sérsic bulges close to the top left corner and the nearly bulgeless galaxies with clear spiral features towards the lower right corner.

Fig. 2 shows the stellar mass distribution of our sample with the median and interquartile range indicated with solid and dotted black vertical lines, respectively. The galaxy stellar mass is calculated summing the stellar masses of all particles inside a sphere of 30 kpc radius and centred on the most bound DM particle. The coloured points and arrows indicate the ranges of different stellar mass estimates for the the MW (Flynn et al. 2006; Licquia & Newman 2015; Bland-Hawthorn & Gerhard 2016; Boardman et al. 2020) and M31 (Tamm et al. 2012; Sick et al. 2015; Boardman et al. 2020).

In the left-hand panel of Fig. 3 we show the best-fitting functions of the two-component decomposition (see Section 2.2.1) for the whole sample of MW/M31-like galaxies. Highlighted with red lines are the best-fitting functions for galaxies with high Sérsic indices. We find that 17.1 per cent of the galaxies in our sample have Sérsic indices $n > 2$. In the following sections, we will explore the physical process, or combination of processes, that drives the evolution of these types of concentrated bulges. We will contrast these results with the evolution of the more abundant systems with flatter SBP. In the right-hand panels of Fig. 3, we show the Sérsic indices, the effective radii and the B/T distributions. All these quantities were derived from the fits to the surface brightness profiles, where B/T is the quotient of the integrals of the Sérsic component and the complete fitted function. The medians are indicated with a black solid line and the interquartile ranges are depicted with dotted lines. The three distributions, with median values of $n_{\rm Sersic} = 1.19$, $r_{\rm eff} = 0.92$, and $\mu_{\rm B/T} = 0.13$, respectively, show a peak skewed towards lower values of and a tail to higher values.

We will see how the Sérsic index and B/T are affected by different aspects of galaxy evolution, so it is important to show that both properties are independent and that we can extract different insights from both of them. The upper panel of Fig. 4 shows that, effectively, the Sérsic index and B/T are not correlated. Notice the low value of the Pearson coefficient that quantifies the grade of correlation in a linear fit. A Pearson coefficient greater that $\mathcal{P} = 0.5$ would imply a significant correlation. Additionally, we show how the two quantities derived from SBPs behave as a function of the stellar mass of the simulated galaxies, to ensure that there is no underlying dependence of our results with stellar mass. The middle and lower panel of Fig. 4 show the Sérsic index and B/T as a function of stellar mass, respectively. Note that neither the Sersic index nor B/T show a correlation with stellar mass, at least in the relatively narrow stellar mass range adopted to select our sample of simulated galaxies. A correlation between Sérsic index and/or B/T with mass could emerge if a wider mass range of simulated galaxies is considered, but such analysis is beyond the scope of this paper and is post-poned to future work.

Finally, we show in Fig. 5 the relation between the B/T obtained from the photometric decomposition and the bulge-to-total ratio derived from the kinematic decomposition of stellar particles ($(B/T)_{\rm kin}$, see Section 2.2.2), as the ratio between the sum of the masses of bulge stellar particles and the total stellar mass of the galaxy, up to the optical radius. The $(B/T)_{\rm kin}$ values are larger on average. Low- and high-Sérsic index bulges show no specific trend in this relation. The values are not expected to be well correlated, although both definitions can give useful insights on the formation of the central regions of galaxies, as we will see later in this work. In a forthcoming paper (Gargiulo et al., in preparation) we will study the link between the kinematical definition of bulges and the photometric definition, described in Section 2.2.1, in detail.

3.1 Does bulge type depend on environment?

We study the influence of environment on the properties of photometric bulges in our sample of simulated galaxies, using the definitions presented in Section 2.2.3. We focus on the Sérsic index and B/T ratio derived as described in Section 2.2.1. As mentioned in Section 1, G19 suggested that the prevalence of low Sérsic bulges in the Auriga galaxies might be, in part, a consequence of the isolation criterion used to select the Auriga DM Haloes for re-simulation. This assumption can be tested with TNG50 in a broader picture, thanks to the larger diversity of environments surrounding our sample of simulated galaxies.

We begin by analysing the dependence of Sérsic index and B/T with the overdensity parameter. In the left-hand panels of Fig. 6, we show the Sérsic index and B/T as a function of the logarithm of the overdensity parameter, considering a number of neighbours $k = 5$, and a mass cut $m_{\rm cut} = 5 \times 10^9$ M$_\odot$ (only galaxies with total masses, i.e. the sum of all types of particles of the subhalo, larger than the cut, are counted). The squares show the median values of the Sersic index and B/T in bins of $\log_{10}(1 + \delta)$. The shaded areas show the standard deviations on each bin. For these particular values of k and $m_{\rm cut}$ we find no significant correlation between Sérsic index, or B/T, with the local overdensity. The middle panel of this figure explores the impact that different values of k and $m_{\rm cut}$ can have on this analysis. These panels show that, independently of the values chosen for these parameters, we find no significant correlation between $n_{\rm sersic}$ and $\log_{10}(1 + \delta)$ and only a very mild correlation with B/T.

As a second test, we measure the local density of galaxies as the number of neighbours inside a sphere of fixed size (see Section 2.2.3).

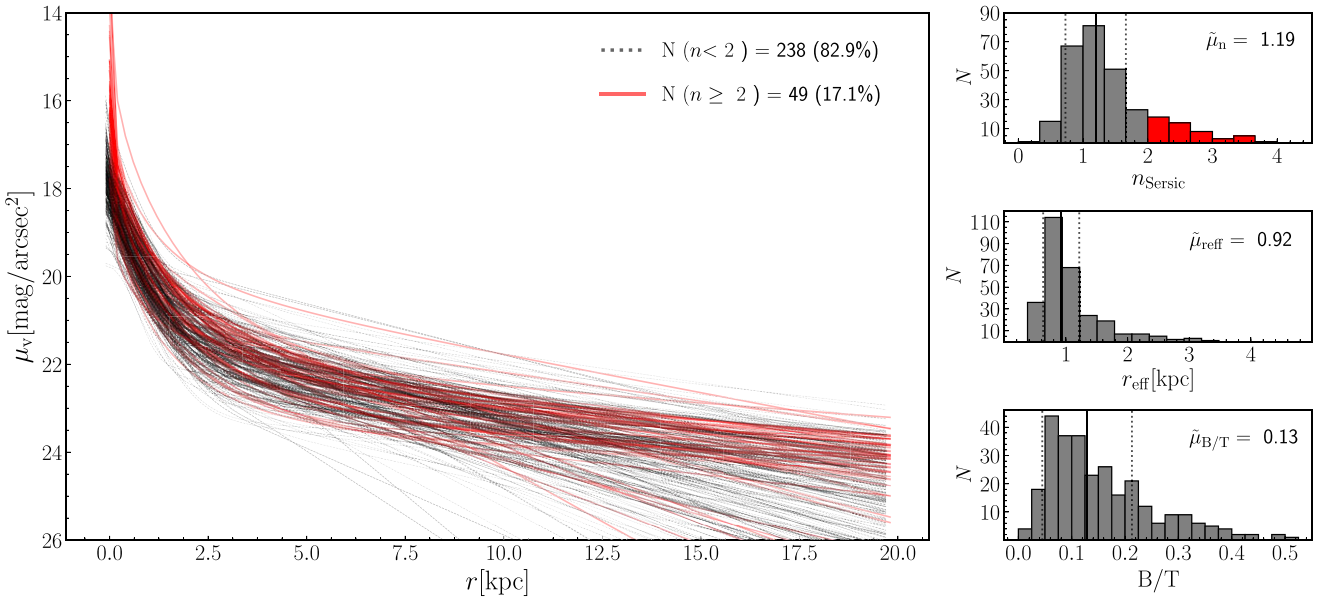

Figure 3. Left-hand panel: Best-fitting functions to the surface brightness profiles of all TNG50 MW/M31-like galaxies of our sample, composed of a Sérsic profile plus an exponential profile (see details on the text). Highlighted with red are the fitting functions with high Sérsic index (17.1 per cent of the sample) that show a concentrated light distribution. Right-hand panels: Distributions of Sérsic index, effective radii, and B/T from the top panel to the bottom panel, respectively. Median values of the distributions are indicated with a solid vertical line and the interquartile range is indicated with dotted vertical lines.

The rightmost panels of Fig. 6 show the dependence of the Sérsic index and B/T on this local density. We find a result similar to the previous one: the Sérsic indices do not correlate with environment as characterized by the number of galaxies that can be found within a sphere of 738.2 kpc radii, while B/T shows a mild correlation towards a higher number of neighbours. This is also independent of the m_{cut} adopted.

Our results strongly point towards a lack of environmental dependence of bulge type in MW/M31-like galaxies. The lack of environmental dependence on these two particular properties of SBPs of galaxies is not surprising. Structural properties of galaxies are shown to be rather independent of the abundance of neighbouring galaxies and more dependent on intrinsic properties like their mass (e.g. Blanton & Moustakas 2009; Peebles & Nusser 2010). More direct observational evidence of this is found in Gao et al. (2018), where no environmental dependence on the properties of bulges of disc galaxies is detected, once the dependence on stellar mass is removed. We acknowledge that, even with the TNG50 simulations, the environmental dependence diagnostics considered in this work may suffer from low number statistics, especially towards larger densities. A larger cosmological volume would be desirable to densely populate all the overdensity bins. Moreover, although TNG50 stands as one the largest efforts to simulate a large cosmological volume with a mass and spatial resolutions comparable with those achieved in the realm of the zoom-in technique, our results may still be influenced by cosmic variance.

4 *IN SITU* AND *EX SITU* COMPONENTS

In this section, we analyse the origin of stellar particles in the central regions of our sample of MW/M31-like galaxies, where photometric bulges arise, dividing them into *in situ* and *ex situ* particles. *In situ* particles are defined as those formed from condensation of the gas that belongs to the host galaxy, while accreted particles are those formed within the potential wells of galaxies that are later accreted on to the main host. This grouping of star particles has been previously used several times in the study of stellar haloes to help understand the kinematics and chemical abundances distribution of their stars (see e.g. Tissera, White & Scannapieco 2012; Tissera et al. 2014; Pillepich, Madau & Mayer 2015; Monachesi et al. 2016, 2019). It has also proven useful to decode the origin of stellar populations in bulges and discs and evaluate how mergers contribute to their formation (Guedes et al. 2013; Gargiulo et al. 2017; Gómez et al. 2017; Fragkoudi et al. 2020, G19). The catalog of *in situ* and *ex situ* particles of the galaxies analysed here was constructed following the considerations in Rodriguez-Gomez et al. (2016).

For this section, to analyse the *in situ* and *ex situ* components of the bulge, we isolate the stellar particles in the inner regions of the galaxies that are not part of the disc, using kinematic information (see Section 2.2.2). As shown by Abadi et al. (2003), bulge components selected by a kinematic decomposition show an increase in surface brightness towards the inner regions, similar to a photometric bulge. Note, however, that it is not possible to unequivocally isolate the particles that constitute a photometric bulge using a kinematic decomposition (see Abadi et al. 2003; Du et al. 2020). This is because the properties of photometric bulges are obtained by decomposing the light distribution in the inner galactic region with two overlapping profiles representing the disc and the bulge. Nevertheless, this type of analysis can give important insights about the physical mechanisms responsible for the formation of different kinds of photometric bulges.

The top panel of Fig. 7 shows the kinematic bulge *ex situ* mass fraction for galaxies with high ($n \geq 2$) and low ($n < 2$) Sérsic index bulges, in red and grey colours, respectively. We can see that high-Sérsic index bulges typically have larger fractions of *ex situ* stars in their kinematic counterpart than low-Sérsic bulges. This is shown by the median values of the distributions, $\tilde{\mu} = 0.09$ and $\tilde{\mu} = 0.28$ for low and high Sérsic bulges, respectively, which are highlighted

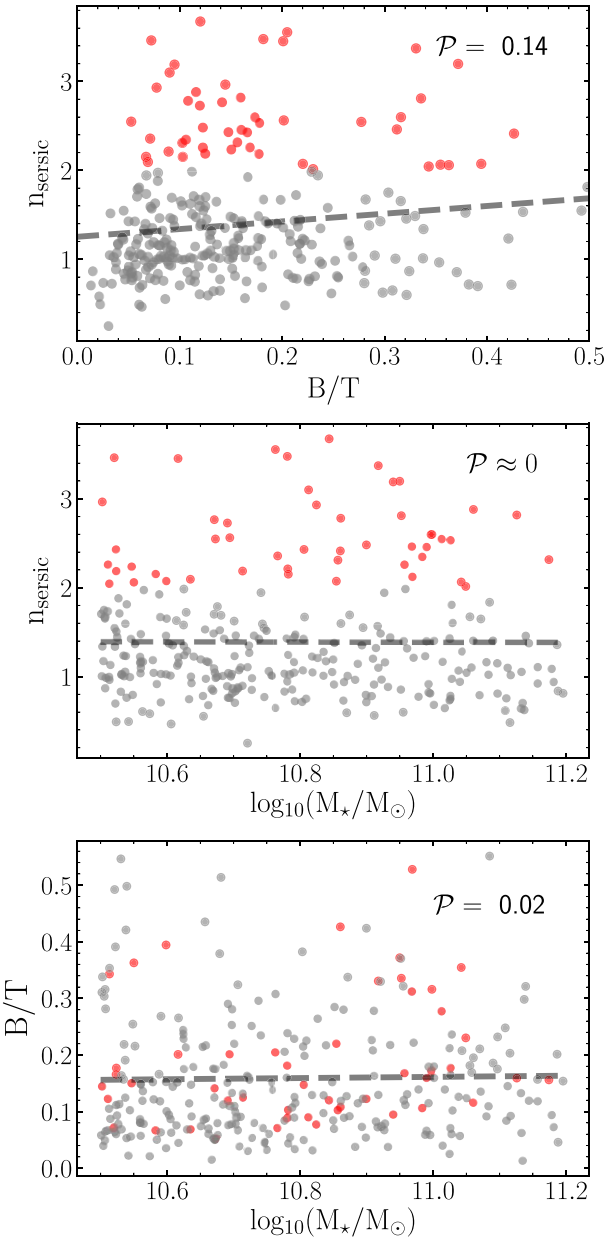

Figure 4. Upper panel: Sérsic index versus B/T for our sample of TNG50 MW/M31-like galaxies, derived from 2-component decompositions to the surface brightness profiles in the *V* band. Simulated galaxies with Sérsic indices above $n = 2$ are highlighted in red. Middle panel: Sérsic index versus stellar mass for our sample of MW/M31-like galaxies. Lower panel: Sérsic index versus stellar mass for our sample of MW/M31-like galaxies. The dashed lines show a least-squares linear fit to the data in the three panels. The value of the Pearson coefficient, that measures the degree of linear correlation, is indicated in the top right corner of each panel. Sérsic index and B/T are independent quantities, and neither of them is correlated with the stellar mass of the simulated galaxies.

with vertical dashed and dotted lines. However, there is no significant linear correlation between Sérsic index and $f_{ex\,situ,\mathrm{bulge}}$. This is shown in the middle panel of this figure, and quantified by the Pearson coefficient. We note here that the accumulation of galaxies with low *ex situ* fractions and low Sérsic index is not dominated by the numerous low-mass galaxies in our sample. In the bottom panel of

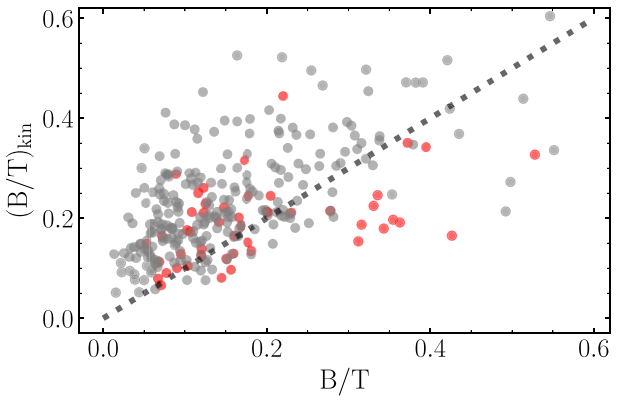

Figure 5. Bulge-to-total ratios derived from the kinematic decomposition (see text and Section 2.2.2) as a function of the photometric B/T (Section 2.2.1). The values for galaxies hosting a high Sérsic bulge ($n > 2$) are indicated in red and for galaxies hosting a low Sérsic bulge ($n < 2$), in grey. The dotted line indicates the 1:1 correlation. These quantities are not expected to be well correlated.

this figure we show the B/T values as a function of the fraction of *ex situ* stars ($f_{ex\,situ,\mathrm{bulge}}$) within the kinematic bulges and find that there is, as well, no correlation. The lack of a correlation of the B/T ratio with the *ex situ* fraction is evident, with a Pearson coefficient value of −0.18. These results indicate that the prominence and concentration of bulges are not trivially related to mergers. Although, it is important to emphasize here that the *ex situ* fraction is not an exact proxy of bulge growth via mergers, since all the stars formed during a starburst triggered by a merger would be considered here as originating *in situ*. The role of mergers in the formation of different kinds of photometric bulges will be the subject of Section 5. Despite the lack of linear correlation between the *ex situ* fraction of stars in the kinematic bulges and the structural parameters of the photometric bulges, an interesting result is that the majority of the kinematic bulges from TNG50 are formed *in situ*, given that the *ex situ* fractions are low for most cases. This is in qualitative agreement with the results found in G19 using the Auriga simulations, which motivates us to compare our results in a more quantitative fashion.

4.1 Comparison with the Auriga simulations

G19 studied the fraction of *ex situ* particles in the central regions of the Auriga simulations and found that the stellar particles of kinematic bulges were formed mostly *in situ*. The Auriga simulations are a suite of high resolution re-simulations of galaxies in MW-sized haloes (Grand et al. 2017), run with the same magneto-hydrodynamic code as the TNG50 simulation, AREPO. However, the physical models used in the simulations differ in the implementation of the AGN feedback and other aspects (see Section 2.1). Moroever, TNG50 was run within a moderately large cosmological box. As a result, we have a MW/M31-like simulated galaxies sample that is ∼7 times bigger than the one used in G19. It is thus worthwile to compare the results of this work with those found in G19 using the Auriga simulations. We now wish to test in a more quantitative way whether the dominance of *in situ* bulges mentioned in the last section is robust and sensitive to changes in the physical model of the TNG50 simulation and to the much larger and more statistically representative sample of galaxies.

The top panel of Fig. 8 shows the density distributions of *ex situ* stellar fraction inside bulges of MW/M31-like galaxies in TNG50

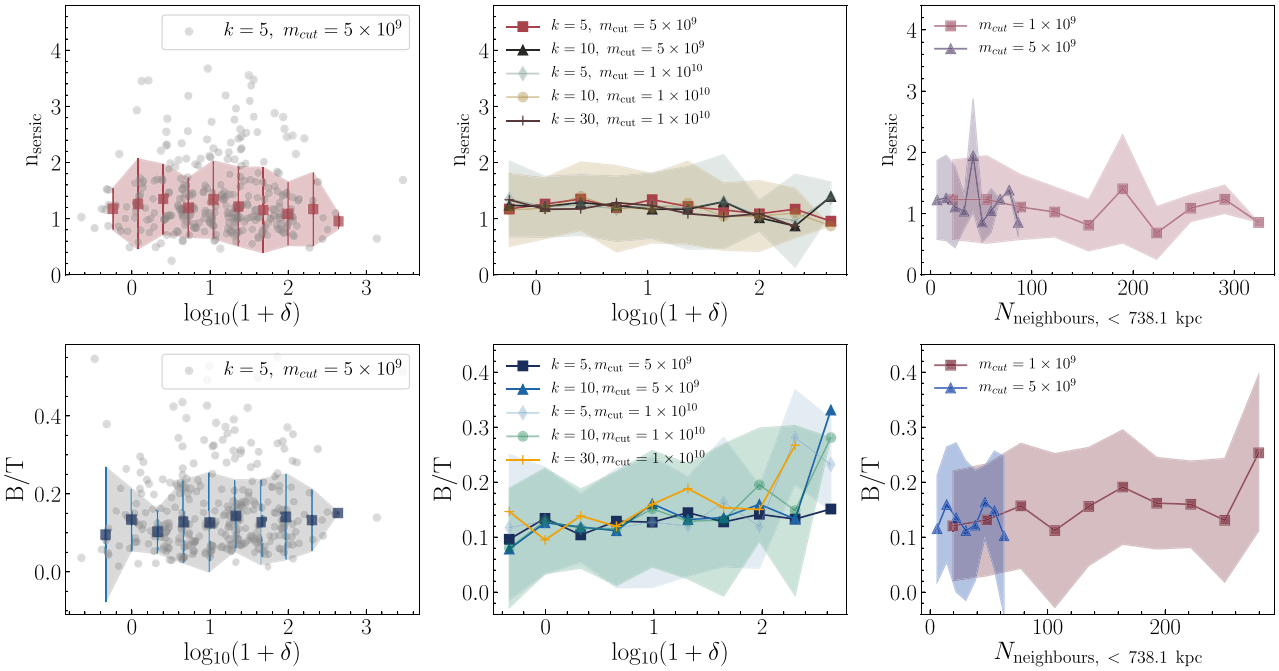

Figure 6. Top left: Sérsic index of bulges in our sample of TNG50 MW/M31-like galaxies, as a function of overdensity parameter (see Section 2.2.3 for the definition) considering $k = 5$ and a stellar mass cut of 5×10^9 $M_\odot$. Dark red squares show the median values in overdensity bins and the corresponding shaded region and errorbars indicate the standard deviation in each bin. Top middle: Medians of Sérsic indices in overdensity bins, for different choices of parameters k and $m_{\rm cut}$ in solar masses, as indicated in the legend. We only show two shaded regions representing the standard deviation in each bin to avoid overcrowding in the plot. Top right: Sérsic index as a function of the number of neighbours inside a 738.1 kpc sphere. Bottom panels: Same as top panels but for B/T values. No measurable dependence of Sérsic index with environment is found and a slight increase of B/T values with overdensity of galaxies can be seen.

and the MW-mass galaxies from the Auriga simulations considered in G19. We take into account only 251 galaxies from our sample of TNG50 simulated galaxies that lie in the same stellar mass range as the Auriga sample, $M_\star\ \epsilon\ [2.75,\ 10.97] \times 10^{10}\,M_\odot$. The kernel density estimations are shown with red and blue lines, for the Auriga and TNG50 simulated galaxies, respectively. The *ex situ* fractions distributions are similar, with a relative excess of bulges with $f_{ex\ situ,\rm bulge} < 0.1$ in the Auriga simulations and the presence of galaxies with very high ($f_{\rm ex\text{-}situ,bulge} > 0.4$) *ex situ* bulge fractions only in the TNG50 sample. To quantify the differences between the distributions we show, in the bottom panel, the cumulative distributions of *ex situ* fractions for both samples of simulated galaxies. A two-sample Kolmogorov–Smirnov statistical test yields a p-value of $p_{\rm KS} = 0.33$, not high enough to discard the null hypothesis, i.e, that both samples come from different distributions. Our results show that the prevalence of *in situ* formed stars in the modelled kinematic bulges, first reported in G19, is confirmed by TNG50. However, statistically, the distributions differ slighly. The low number of galaxies in the Auriga sample relative to the TNG50 sample may play a role, as well as the different median masses of both samples, which are 6.07×10^{10} and 5.09×10^{10} $M_\odot$ for the Auriga and the restricted TNG50 sample, respectively. But, given that the mass range of galaxies was constrained to be the same in both samples, it is fair to assume that the differences in the distributions come, at least partially, from the differences in the galaxy formation models. The AGN model implemented in TNG50 (see Section 2.1) might prevent to some degree the formation of stars in the central regions (see also Nelson et al. 2021), and elevate the fraction of *ex situ* stars with respect to the Auriga simulations. Another noteworthy fact is that in the Auriga sample G19 did not find any high-Sérsic bulge, differently from the restricted TNG50 sample, where 17.5 per cent of the galaxies host a high-Sérsic bulge. The low number of galaxies in the Auriga sample, with respect to the restricted TNG50 sample, prevents us to draw further conclusions on this fact.

An interesting aspect regarding the *ex situ* component of the kinematic bulges, and also studied by G19, relates to the number of satellites that contributed to the majority of their *ex situ* stellar component. Fig. 9 shows donut charts displaying the number of satellites needed to add-up 50 and 90 per cent of the total *ex situ* stellar mass in the kinematically selected bulges of our TNG50 MW/M31-like sample. We find that $\sim$ 76.8 per cent of the galaxies have bulges in which half of the *ex situ* component was contributed by a single accretion event. For the remaining, we find that in 17.7 and 5.4 per cent of the galaxies half of the *ex situ* component was brought to the bulge by two and three or more satellites, respectively. To build up 90 per cent of the *ex situ* mass of the kinematic bulge we find that less than four satellites are sufficient in 67.2 per cent of the cases, with a median value of two satellites. These results are in line with those obtained in G19 with the Auriga simulations, where only a few satellites (a median of 3 satellites) account for 90 per cent of the *ex situ* component of kinematically selected bulges and, in most cases (with a median value of one satellite), the stellar particles of one single satellite dominate the *ex situ* component (i.e. this satellite accounts for more than 50 per cent of the total *ex situ* stellar particles in the kinematic bulge).

5 ROLE OF MERGERS

In this section, we further explore the relation between bulge properties and merger events. In the left-hand panel of Fig. 10, we

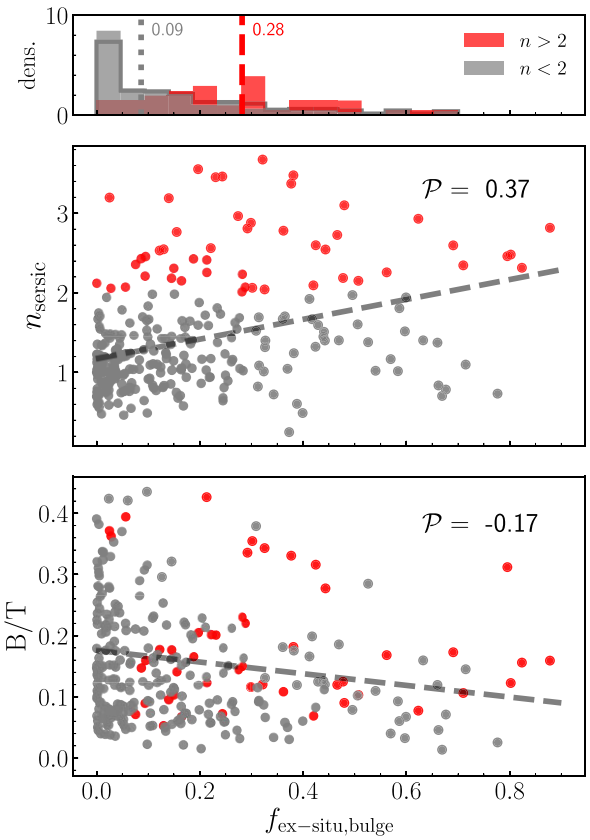

Figure 7. Top panel: Distributions of the *ex situ* fractions of stars in kinematic bulges of TNG50 MW/M31-like galaxies with high- and low-Sérsic indices in red and grey, respectively. Median values are indicated with grey dotted and red dashed lines. The median of the *ex situ* fraction distribution of high-Sérsic bulges is significantly larger than the one for low-Sérsic bulges. Middle panel: Sérsic index as a function of *ex situ* fraction of stars in kinematic bulges. Galaxies with high-Sérsic index are highlighted in red. The dashed grey line is the best-fitted linear function using a least-squared method. The Pearson coefficient of the linear adjustment is shown in the legend. The Sérsic index and the fraction of *ex situ* stars in the kinematic bulges are linearly uncorrelated, according to this metric, in our sample of MW/M31-like galaxies. Bottom panel: B/T as a function of *ex situ* bulge fraction. There is a null correlation between the *ex situ* fraction of stellar particles in kinematic bulges, and the excess of light in the central regions of our sample of simulated galaxies.

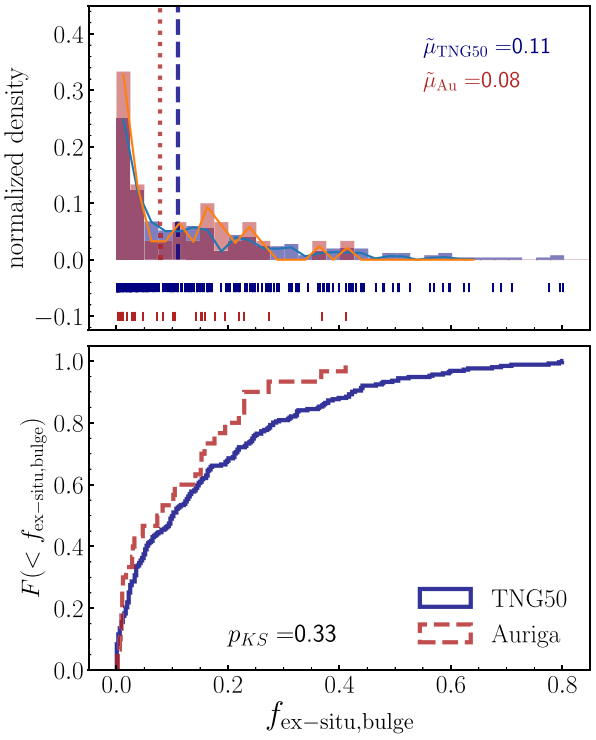

Figure 8. Top panel: Normalized density of *ex situ* fractions in bulges of a sample of 30 MW–mass galaxies of the Auriga simulations (red), compared with *ex situ* fractions of a subsample of TNG50 MW/M31-like galaxies (blue), selected to be in the same mass range. Solid lines are kernel density estimations of the distribution for both simulations. The red dotted and blue dashed line indicate the median values as indicated in the legend. Blue and red short lines in the bottom of the figure show the individual values in the distribution. Bottom panel: Cumulative distributions of the *ex situ* bulge fractions for both simulations. The *p*-value of a two-sample Kolmogorov–Smirnov statistical test is also shown. Both simulations show a similar distribution of accreted stellar fraction in kinematic bulges, but statistically differ due to differences in the physical model.

show the Sérsic index as a function of the total number of significant mergers, $N_{\rm mergers}$, experienced by our TNG50 sample of MW/M31-like galaxies. Here we only consider mergers with mass ratios $m_{\rm ratio} = m_{\rm tot,sat}/m_{\rm tot,host} > 0.1$, since redshift $z = 12$ up to present day, where $m_{\rm tot,sat}$ and $m_{\rm tot,host}$ are the total mass of the merging satellite and the host galaxy, respectively. The black line represents the median value per bin and the shaded region the interquartile range. Note that the $N_{\rm mergers}$ does not account for the diversity in the merging history of galaxies, since mergers with different mass ratios, and at different times, are counted in this variable. In the right-hand panel of Fig. 10, we now show the total accreted mass (i.e. DM, gas, and stars) from those significant mergers (i.e. $m_{\rm ratio} > 0.1$) by each MW/M31-like galaxy as a function of Sérsic index. Although the median values in both diagrams show an increase towards larger number of mergers and total accreted mass, the number of simulated galaxies in the last bins is too low, and most galaxies with high Sérsic index show a moderate number of significant mergers (3–8) and total accreted mass (20–150 $\times$ 10^{10} $M_\odot$). All in all, we find no significant correlation between merging history measured in this way and Sérsic index.

The timing of mergers may play a role in shaping the surface brightness profile of a galaxy. A late merger is more likely to induce recognizable perturbations on the host's present-day stellar kinematics than an early event since secular processes have less time to act and reconfigure the galactic phase-space distribution. Moreover, physical conditions, such as the availability of gas supply to form stars in a burst, are different at different stages of a galaxy's evolution. As a result, although the build-up of the light profile of galaxies is a complex and cumulative process, either the last significant accretion event, or the most massive merger a galaxy has experienced, are more likely to leave a visible imprint in the resulting light profile at $z = 0$ than other events.

We will now focus on the characteristics of the last significant merger experienced by each galaxy. The bottom panel of Fig. 11 shows the Sérsic index of the photometric bulges as a function of look-back time ($t_{\rm lb}$) of the last significant merger, $t_{\rm lb}^{\rm lsm}$ (i.e. with merger ratio $m_{\rm sat}/m_{\rm host} > 0.1$). Here, the time of the merger is defined as the look-back time of the snapshot at which the satellite (or secondary progenitor), is no longer identified by the SUBFIND algorithm. Our goal is to better identify the instant of time when the

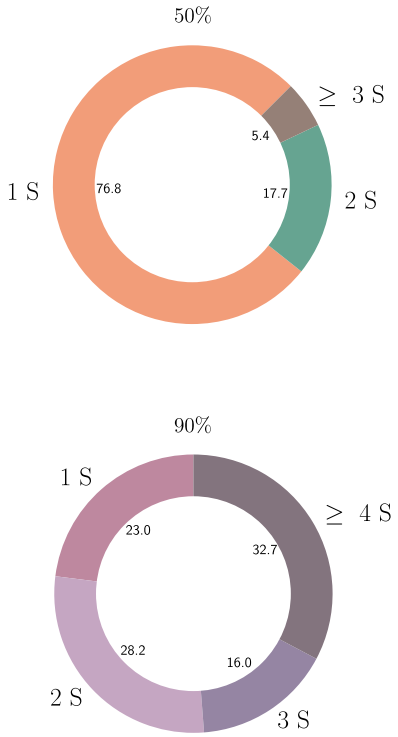

Figure 9. Fractions of simulated TNG50 MW/M31-like galaxies in our sample that need the indicated number of satellites to build-up 50 per cent (top chart) and 90 per cent (bottom chart) of the total *ex situ* stellar mass of kinematically selected bulges. A single satellite is enough to explain the majority of the accreted mass budget in bulges. Only a few of them are enough to sum almost the total of the accreted stars.

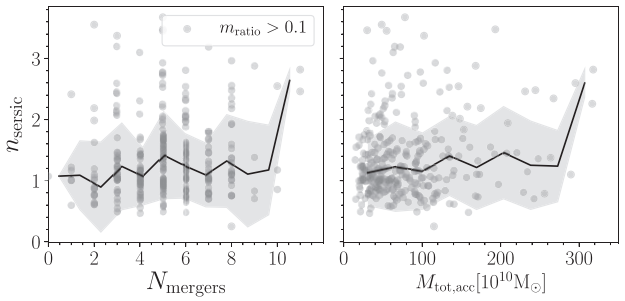

Figure 10. Left-hand panel: Sérsic index as a function of the number of mergers experienced by each TNG50 MW/M31-like galaxy with merger ratio $m_{\rm ratio} > 0.1$. Right-hand panel: Sérsic index as a function of the total mass accreted in mergers with merger ratio $m_{\rm ratio} > 0.1$. The black line represents the median value per bin and the shaded region the interquartile range. The number of mergers and total accreted mass in mergers in galaxies have no measurable effect in the Sérsic index of bulges.

merger could have a stronger effect on the surface brightness profile of the host. The mass ratio, however, is measured at the time when the satellite reaches its maximum stellar mass, because a substantial amount of loose particles that belonged to the satellite are assigned to the central galaxy by the halo finder, which results in a significant underestimation of the merger ratio. This, in turn, adds a resolution dependent effect, since in simulations with better resolution a satellite takes longer to merge (see section 5.2 in Rodriguez-Gomez et al. 2015).

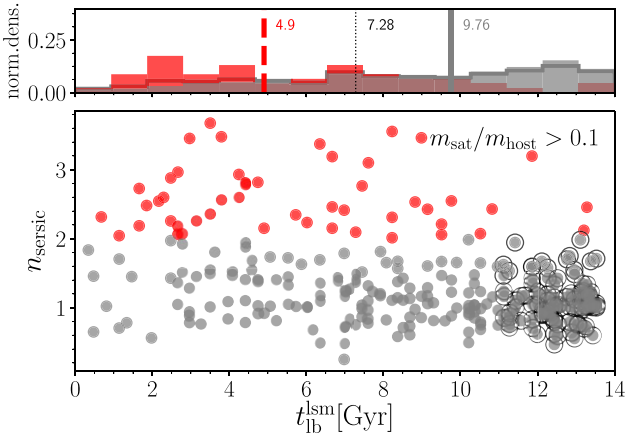

Figure 11. Top panel: Distribution of look-back time of the last merger with $m_{\rm tot,sat}/m_{\rm tot,host} > 0.1$, $t_{\rm lb}^{\rm lsm}$, for galaxies with high-Sérsic and low-Sérsic photometric bulges, in red and grey, respectively. Median values of the distributions are shown alongside the filled grey line and a dashed red line. A dotted black line indicates the median value of the $t_{\rm lb}^{\rm lsm}$ distribution of simulated galaxies hosting low-Sérsic bulges when extremely early last mergers ($t_{\rm lb}^{\rm lsm} > 11$ Gyr) are not considered. Bottom panel: Sérsic index as a function of $t_{\rm lb}^{\rm lsm}$. Grey indicates simulated galaxies with low-Sérsic photometric bulges and red indicates those with high-Sérsic bulges. Highlighted with black circles are galaxies with low-Sérsic bulges that experienced the last significant merger more than 11 Gyr ago. Galaxies hosting a high-Sérsic bulge experience the last significant merger at substantial later times, on average.

On average, galaxies hosting high-Sérsic photometric bulges experienced the last significant merger at later times than galaxies with low-Sérsic bulges. The distribution of $t_{\rm lb}^{\rm lsm}$ is shown in the top panel. The low- and high-Sérsic index population have median $\tilde{t}_{\rm lb}^{\rm lsm} = 9.764$ and $\tilde{t}_{\rm lb}^{\rm lsm} = 4.9$ Gyr and are indicated with a filled grey line and red dashed line, respectively. Note, however, that a significant group of simulated galaxies with low-Sérsic bulges, highlighted in Fig. 11 with black circles, did not experience a merger with $m_{\rm tot,sat}/m_{\rm tot,host} > 0.1$ during the last 11 Gyr. These galaxies have undergone a very quiet merger history over their entire history. If we do not consider this group of galaxies, the low-Sérsic distribution shows a median value of $t_{\rm lb}^{\rm lsm} = 7.28$. This result indicates that there is a link between the occurrence of a late merger and the concentration of the surface brightness profile. Although there is no linear correlation between the Sérsic index of photometric bulges and the time of the last significant merger suffered by the simulated MW/M31-like galaxies, the median value of $t_{\rm lb}^{\rm lsm}$ is higher for galaxies with high Sérsic index bulges. A similar analysis taking into account the most massive merger of each simulated galaxy showed no correlation with this particular event and the Sérsic index of photometric bulges, with similar distributions of $t_{\rm lb}$ of the most massive merger for low- and high-Sérsic bulges.

Another noteworthy property of galaxies that may affect the outcome of mergers is the gas fraction at the moment of the interaction. We define the gas fraction, $f_{\rm gas}$, as the ratio between the mass in cold gas and the stellar mass of the host galaxy at the time of peak mass of the satellite (the same instant of time that we use to define the merger mass ratio). To measure the amount of cold gas we sum the mass of gas in cells defined as *star forming* in the simulation, i.e. the gas cells that are above the star formation threshold for the Springel & Hernquist (2003) ISM model. We show in Fig. 12, the Sérsic index as a function of the logarithm of the gas fraction, at

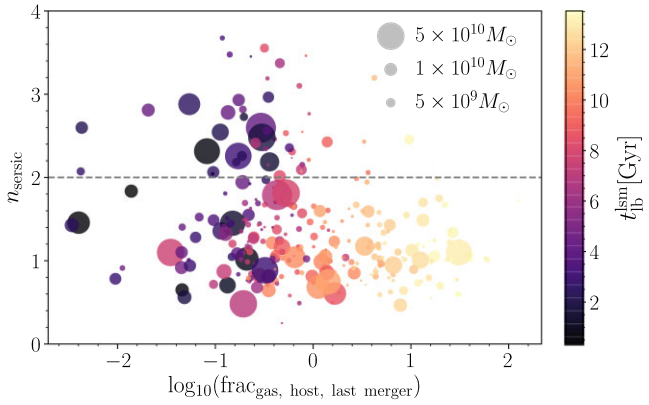

Figure 12. Sérsic index as a function of the logarithm of the host gas fraction at the time of the last significant merger ($m_{\rm tot,sat}/m_{\rm tot,host} > 0.1$). The colour coding indicates the look-back time of the last merger and marker sizes are indicative of the stellar mass of the accreted satellite in the last merger. Gas-poor mergers in the late Universe are not exclusive of galaxies with high-Sérsic bulges. Early gas-rich mergers are exclusive of galaxies with low Sérsic bulges.

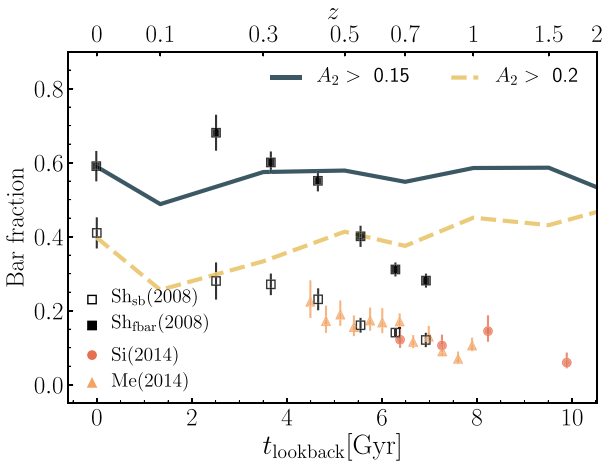

Figure 13. Bar fraction as a function of lookback time. Bar fractions computed for the simulated sample of TNG50 MW/M31-like galaxies are subject to a minimum V-band luminosity threshold (see text) at $z = 0$, together with the direct progenitor of each at $z > 0$. Two different thresholds of bar strengths to classify a galaxy as barred are shown, as indicated in the legends. Observational estimates of bar fractions from Sheth et al. (2008) are shown with filled black squares and empty black squares. Empty squares correspond to strong bars. Dark orange circles are from Simmons (2014) and orange triangles are from Melvin et al. (2014). Bar fractions in the progenitors of our sample of MW/M31-like galaxies do not decrease with redshift. No direct comparison of observations and simulations is suggested, as the galaxy samples selected – as well as the methods for identifying bars – differ between the two.

the time of the last considerable merger ($m_{\rm tot,sat}/m_{\rm tot,host} > 0.1$). The colour coding indicates the $t_{\rm lb}^{\rm lsm}$ of this last merger and the size of the circle is proportional to the stellar mass of the accreted satellite. The gas fraction clearly correlates with the $t_{\rm lb}^{\rm lsm}$, as is expected because of the exhaustion of the gas supply of galaxies with time. We can see that a group of galaxies with low Sérsic index with no significant mergers through most of their history accreted low-mass satellites at early times in a very wet merger, that is, with a high fraction of cold gas available, larger than unity. High Sérsic bulges had predominantly mergers with gas fraction between unity and a tenth, but there is no clear correlation between the gas fraction and the concentration of bulges. Many low-Sérsic bulges show the same pattern as high-Sérsic bulges. Looking at the mass of the satellite galaxy reflected in the sizes of circles we can tell that there is also no correlation with the behaviour of galaxies with low and high-Sérsic bulges, except for the fact that there is a large group of low Sérsic galaxies that do show a last merger with low mass satellites, with high gas fractions that occurred at early times.

The lack of clear correlations with the properties of mergers and the Sérsic index of bulges does not necessarily mean that mergers have a low impact on the formation of bulges. The fact that the *ex situ* fraction in kinematic bulges is higher more frequently in high Sérsic bulges (see Fig. 7) is the first indication that mergers play a role. Mergers are ubiquitous in the current paradigm of galaxy formation and the fact that some large galaxies in the Local Group and the MW galaxy itself show no signatures of a merger-built bulge component (although see Kunder et al. 2016) has led to the idea that there is a tension of the paradigm with observations (e.g. Shen et al. 2010). In G19, it was found that despite the rich merger histories of simulated MW-mass galaxies, kinematically selected bulges were formed mostly *in situ* and show properties more akin to pseudo-bulges. Here we see that on one side, there are MW/M31-like simulated galaxies that do not suffer a significant merger since the very early epoch of their formation. On the other side, mergers evidently do not always reach and affect the central region of the galaxy. In the following section we explore other relevant physical mechanisms that could play a significant role in the formation and evolution of bulges, modulating the effects associated with merger events.

6 INFLUENCE OF BARS

In this section, we analyse the influence of bars on the shape of the bulge surface brightness profile, characterized by the Sérsic index and B/T.

6.1 Bar demographics

We first check the evolution of the bar fraction in our sample of MW/M31-like galaxies. Fig. 13 shows the fraction of barred galaxies in a subsample of TNG50 galaxies as a function of $t_{\rm lb}$, together with different observational estimates of the bar fraction in $\sim L_\star$ galaxies as a function of $t_{\rm lb}$. Sheth et al. (2008) measured bar fractions in the COSMOS survey (Scoville et al. 2007). The existence of a bar is determined by the ellipse fitting method (Menéndez-Delmestre et al. 2007), which consists in following the excess in the ellipticity profile up to a sudden change in the position angle profile of the fitted ellipses. They report two different estimates of bar fraction based on the ellipticity of the isophotes. One is simply referred to as the bar fraction ($f_{\rm bar}$), and takes into account all bar detections. The other is estimated considering only bars with ellipticities greater than 0.4, and named the strong bar fraction (sb). The total bar fraction is shown with black filled squares, and the strong bar fraction is shown with empty black squares. Orange triangles show the bar fraction estimates of galaxies in the COSMOS survey, but based on the visual classification of the Galaxy Zoo project from Melvin et al. (2014). Dark orange circles show the observational data from Simmons (2014) who estimated the fraction of galaxies with strong bar features in the Galaxy Zoo (Lintott et al. 2008) using galaxies from the CANDELS survey (Koekemoer et al. 2011) up to $z = 2$. Observational estimates rely on the selection of galaxies at different redshifts that are brighter than the $M_V^\star$ region of the rest-frame

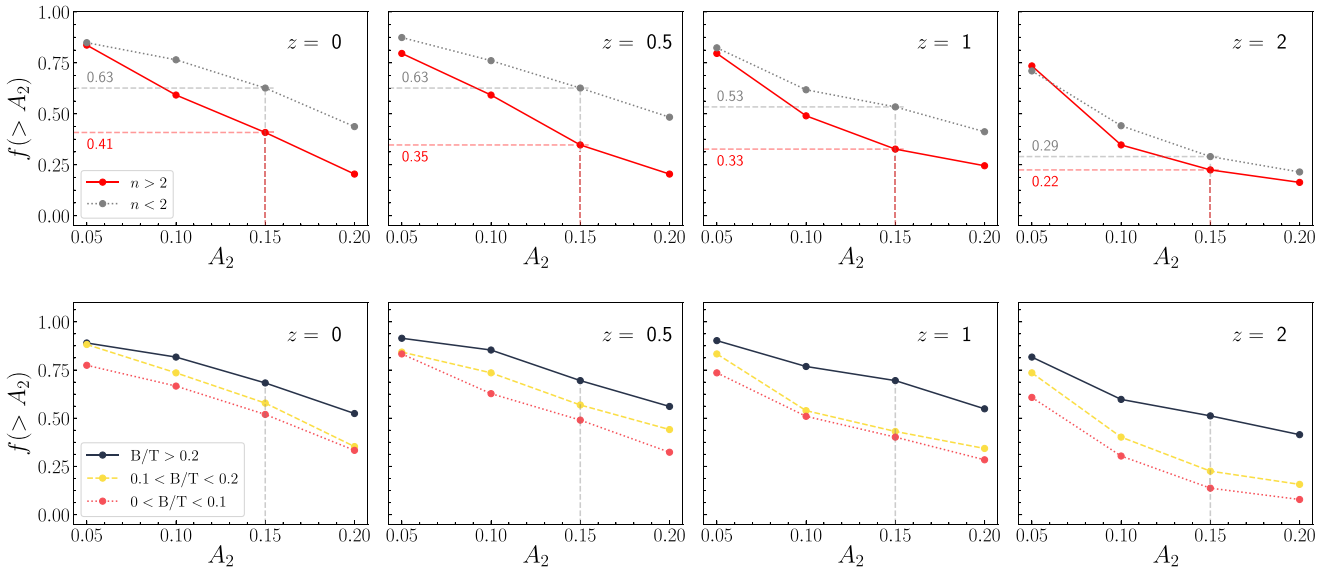

Figure 14. Top panels: Cumulative fraction of bar strengths of TNG50 MW/M31-like simulated galaxies with high- and low-Sérsic indices in their bulges at $z = 0$ are shown as red solid lines and dotted grey lines, respectively, at four different redshifts, as indicated in the legends. An excess of bars in the progenitors of galaxies with low-Sérsic bulges at $z = 0$ is present at all redshifts since $z = 2$. Bottom panels: Cumulative fraction of bar strengths in TNG50 MW/M31-like simulated galaxies in three intervals of B/T as indicated in the legends. Progenitors of galaxies with larger B/T at $z = 0$ show a higher bar fraction at all cosmic epochs, highlighting the influence of bars in the formation of photometric bulges.

luminosity function at higher redshifts. The $M^{\star}_V$ parameter as a function of redshift was estimated in Marchesini et al. (2012), by fitting a Schechter function to the rest-frame luminosity functions in the *V* band at redshifts $z = [0.55, 0.90, 1.30, 1.8, 2.4, 3, 3.64]$. Later on, a parametrized curve is fitted to the observed $M^{\star}_V$ values as a function of redshift. We follow the progenitors of simulated galaxies in our sample at $z = 0$ using the merger trees from the simulation. By means of the parametrized curve fitted to the observed $M^{\star}_V$ we impose this magnitude threshold to our sample of galaxies at each redshift. Observations also establish different selection criteria of strong barred galaxies than simulations. To take this into account, we consider two different thresholds in the amplitude of the second Fourier mode A_2 to consider a galaxy as barred. One of the caveats of the comparison is that we quantify bar strength and length based on the stellar mass distribution, whereas observationally this depends of the photometric band used for the analysis. Moreover, the definition of barred galaxies in an observational sample is based on visual inspection or the ellipse fitting method. Overall, the methods to estimate bar fractions of galaxies in observations and simulations and the sample selection differ considerably, and both present limitations, so a direct comparison between observed estimates of bar fractions and those obtained in our simulated galaxies is not intended. However, we find it useful to show the observational estimates to guide the reader in the following argument. The observed fractions of barred galaxies show a decrease after $z \sim 0.4$, in all cases. The bar fraction of the progenitors of galaxies in our sample do not decrease toward higher redshifts. This apparent excess of barred galaxies in our sample at high redshifts might contribute to the excess of low-Sérsic bulges that we see in our sample of MW/M31-like galaxies compared with observations, as we later discuss in Section 7. Nevertheless, we caution once again that a better and more quantitatively meaningful comparison between simulations and observations is required to clearly assess the degree of this apparent discrepancy. For example Rosas-Guevara et al. (2021) study the evolution of the bar fraction of galaxies in TNG50 and faced the same limitations. When considering only bars larger than 2 kpc in TNG50, which is a typical resolution limit in images used to measure bars in observations at high redshift, the bar fractions show a decrease with redshift that is qualitatively similar to what observers find.

6.2 Bar evolution

We now concentrate on the evolution of the bar strengths to investigate the effect that bars may have on the morphology and formation of photometric bulges. The top panels of Fig. 14 show the cumulative fraction of galaxies with bars stronger than a given A_2 value. Galaxies with high- and low-Sérsic bulges are shown with red and grey lines, respectively. Different panels show results at different redshifts. As shown in the top leftmost panel, at $z = 0$ there is a clear excess of bars in simulated galaxies with low Sérsic index. At $z = 0$, 63 per cent of simulated galaxies with low-Sérsic index have a noticeable bar, stronger than $A_2 = 0.15$ and only 41 per cent of those with high-Sérsic index show bars with that magnitude. As we move to higher redshifts, the relative difference of bars with strength $A_2 > 0.15$ remains large, reaching a maximum difference of 0.28 at $z = 0.5$. At $z = 2$, bar fractions drop significantly for both sub-samples. Notice that this bar fraction evolution is not evidenced in Fig. 13 because we only consider galaxies more luminous than $M^{\star}_V$ at each redshift in that case. In the bottom panels of Fig. 14 we now divide the sample of galaxies based on the parameter B/T. The red, yellow, and black lines show the cumulative number of galaxies as a function of A_2 for galaxies with $0.0 < B/T < 0.1$, $0.1 < B/T < 0.2$, and $B/T > 0.2$, respectively. We can see that across all redshifts, and for all bar strengths considered, galaxies with larger B/T values show a greater fraction of bars than less luminous bulges. This indeed suggests a correlation between bulge prominence and the prevalence of bars.

The results found here are qualitatively in agreement with those shown by Weinzirl et al. (2009), who found that 65 per cent of

their sample of bright spirals with low Sérsic index are barred, whilst 38 per cent of them with high Sérsic index ($2 < n < 4$) have bars. However, a one-to-one comparison is not possible for two main reasons. First, their galaxy sample spans a wider range in mass and, secondly, they include a bar component in their 2D surface brightness decomposition. The addition of a bar component is probably the main reason for a disagreement in the trend found in our results of bar fraction for different ranges of B/T; Weinzirl et al. (2009) found that galaxies with lower B/T are most likely barred. Galaxies with B/T < 0.2 have a high bar fraction of ~ 68 per cent, and those with $0.2 <$ B/T < 0.4 and B/T > 0.4 have bar fractions of ~ 42 and ~ 17 per cent, respectively. The trend exhibited by their results is opposite to what we find in our simulated galaxies, where a bar component in the surface brightness profile decomposition is not included. When a bar is considered as a separated entity, a significant fraction of the light associated with the bulge in a two-component fit would be associated to the bar component. This effect can be readily seen comparing the results of G19, with those of Blázquez-Calero et al. (2020), who analysed the same sample of the Auriga simulation suite and applied two-component light decompositions and three-component light decompositions (including a bar component), respectively. The B/T ratios derived by G19 are consistently larger than those obtained by Blázquez-Calero et al. (2020). The implications of these results are discussed in Section 7.

6.3 On the bulge-bar connection

Bars are not always persistent features. Is it fair to assume that the duration of a bar feature would determine the influence of this component on the evolution of a galaxy and, in particular, its photometric bulge. To quantify the period of time during which a given galaxy contained a significant bar we proceed as follows. First, we define a bar strength threshold $A_{\rm thresh}$. We then search for all those snapshots in the simulation where $A_2 > A_{\rm thresh}$. At every snapshot, S_i, where $A_2 > A_{\rm thresh}$, and due to the relatively poor time resolution, we assume that the bar has been above $A_{\rm thresh}$ for a period equal to $[t_{\rm lb}(S_{i-1}) - t_{\rm lb}(S_{i+1})]/2$. Finally, the total time a bar has had an amplitude above $A_{\rm thresh}$ since $t_{\rm lb} < 10$ Gyrs is computed as

$$t_{(>A_{\rm thresh})} = \frac{1}{2} \sum_{i_{>A_{\rm thresh}}} \left([t_{\rm lb}(S_{i-1}) - t_{\rm lb}(S_{i+1})] \right), \quad (9)$$

where $i_{>A_{\rm thresh}}$ counts over the snapshots where the amplitude of the second Fourier mode is larger than $A_{\rm thresh}$.

In the top panel of Fig. 15, we show the dependence of Sérsic index of our simulated galaxies with the period that a system hosted a strong bar with $A_2 > 0.2$. The colour coding indicates the fraction of *ex situ* stars in each bulge. We find no correlation between Sérsic index and the duration of a strong bar (top panel). However, it is interesting to see how different regions in this diagram are populated. Galaxies with high-Sérsic index bulges typically do not develop strong bars during most of their evolution, as was already hinted in Fig. 14. There are a dozen galaxies with high-Sérsic bulges that developed a bar during more than 3 Gyr in their history, some of them with Sérsic indices close to the threshold imposed to divide them into low- and high-Sérsic bulges. Most of the bulges with long-lived bars ($t_{>A_2} > 3$ Gyr) show either low or negligible *ex situ* fractions in the kinematic bulge, as well as low Sérsic bulges. Galaxies with short-lived bars, on the other hand, show both low- and high-Sérsic index bulges. Among those, the galaxies with high-Sérsic index bulges commonly show high *ex situ* fractions, as already shown in Fig. 12.

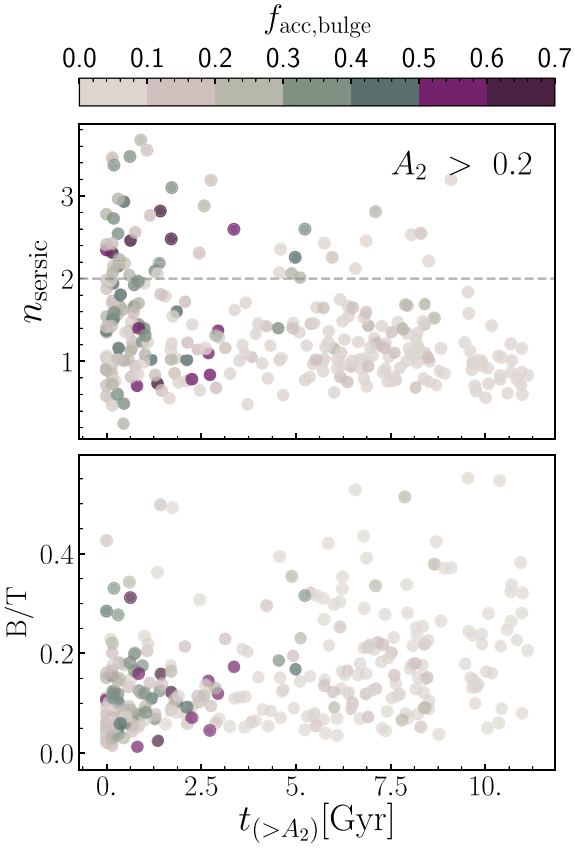

Figure 15. Top panel: Sérsic index as a function of the duration of the bar, colour coded with the fraction of *ex situ* stars in the bulge, for our sample of simulated TNG50 MW/M31-like galaxies. Bottom panel: B/T as a function of the duration of the bar with the same colour coding as in the top panel. High-Sérsic bulges usually develop in galaxies that do not host a bar for a long time.

The bottom panel of Fig. 15 shows the B/T ratio as a function of strong bar duration with the same colour coding as in the top panel. There is no clear correlation between the photometric B/T ratio and the duration of the bar, but two broad main branches can be seen in this panel, departing from the locus of points with low B/T and short-lived bars, i.e B/T < 0.1 and $t_{(>A_2)} < 3$ Gyr. On one hand, we see galaxies with long-lived strong bars that in some cases show significant values of B/T, larger than B/T $= 0.15$. These likely grew their photometric bulges through bar-related processes. On the other hand, there are galaxies with short lived bars that also present large values of B/T. Some of them show higher *ex situ* fractions in their kinematic bulge, thus, in this case, also mergers likely contributed to grow their photometric bulges.

7 DISCUSSION

We have studied the formation of bulges in a sample of galaxies of MW/M31-like galaxies drawn from TNG50. In this section, we discuss our findings in general and in relation to the current understanding about the role that mergers and bars can play in the formation and evolution of bulges.

By means of 1D, two component photometric decompositions of the surface brightness profiles of our sample of MW/M31-like galaxies we find that 17.1 per cent have Sérsic indices $n_{\rm sersic} > 2$, i.e. very concentrated bulges components, consistent with the

structure expected for classical bulges. An interesting question to address would be if this fraction of classical bulges is consistent with the fraction of concentrated photometric bulges estimated from observations. Fisher & Drory (2011) compiled a set of ≈100 observations of galaxies in a local 11 Mpc volume, obtained with a consistent methodology, and produced a census of bulge type as a function of the stellar mass of galaxies. They found that, for galaxies with stellar masses in the range defined by our sample ($\log_{10}(M_\star) \in [10.5, 11.2]$), ∼ 50 per cent of bulges can be classified as classical, which have Sérsic index $n > 2$ almost in all cases. This proportion is higher than the 17.1 per cent of concentrated bulges found in this study. Note however that the observed sample of galaxies has a low number in the mass range considered in our work, and also include elliptical galaxies in the classical bulge classification; the latter are excluded from our analysis. Another possibility is that the TNG50 simulation is underproducing high Sérsic index bulges, when compared with MW-mass galaxies in the local Universe. However, it is not possible to draw a definitive conclusion from the analysis presented in this work. A more precise answer to this question must be addressed in a new study, in which the same galaxy selection criteria are applied for both the observed and simulated sample of galaxies.

It has been pointed out in previous works that the overabundance of galaxies with low-Sérsic bulges can be a resolution issue, via two main channels (Martig et al. 2012): Bois et al. (2010) showed that dynamical resolutions near 32 pc are needed to correctly remove angular momentum in mergers and produce slowly rotating ellipticals. Although the TNG simulations are successful in producing slowly rotating ellipticals (e.g. Pulsoni et al. 2020), it is fair to speculate that a higher resolution might still be needed to correctly redistribute angular momentum in the central regions of disc galaxies, thus producing more concentrated bulges supported by anisotropy. Additionally, using zoom-in simulations, Sparre & Springel (2016) showed that simulations with higher resolutions than Illustris (similar to TNG100 and hence 16 times worse in particle mass than TNG50) are more efficient to produce starburst in galaxy mergers. With TNG50 we show that bursts of star formation are prominent during the phases of gas-rich mergers of MW/M31-like galaxies (Still et al., in preparation), yet it is unclear to what degree this is converged and particularly so for the question of bulge formation.

Secondly, the lack of accuracy in the follow-up of the fragmentation of gas in the early evolution of the galaxy might suppress a bulge formation channel, through formation of gas clouds that sink into the central parts of a galaxy due to dynamical friction (Dekel et al. 2009; Ceverino et al. 2010; Perez et al. 2013). This process is thought to contribute mostly to form concentrated bulges.

The resolution analysis shown in Appendix A suggests that convergence on the SBP of these late type simulated galaxies is only starting to be reasonably achieved at the resolution level of TNG50-1. This is in good agreement with the results presented in Grand et al. (2021), where they studied this problem considering two higher resolution levels, all in the context of the Auriga project. They show that surface density profiles of MW-mass galaxies are starting to be well converged at resolution levels of 5.4×10^4 $M_\odot$ in the baryonic component, which is comparable to the TNG50-1 resolution. It is worth highlighting, however, that lower resolution levels than that associated with TNG50-1 will suffer from this issue. For example, Du et al. (2020) analysed the TNG100-1 simulation, with a mass resolution 16 times worst than the one considered here, and found only a few galaxies with concentrated bulges.

None the less, simulations like TNG50-1 studied in this work, with a minimum gravitational softening of ∼300 physical pc for the stars, are a major step in understanding the physical processes that contribute to form the diversity of bulges found in MW/M31-like galaxies in the local Universe.

Another issue worthy of attention and recently discussed by Peebles (2020b) is the relative scarcity of very low B/T bulges in state-of-the-art cosmological simulations compared to a local sample of observed galaxies with $L \backsim L_\star$. The discussion is based on a comparison between the hot kinematical state of particles in simulated galactic components and the observed values of the rotational degree of the components of nearby galaxies. It was also shown, however, that when taking into account B/T_V ratios, which are derived from surface brightness profiles of simulated galaxies in the *V* band (G19), the resulting B/T_V distribution in simulated galaxies is comparable to the observed distribution of B/T. We find that the median of the B/T distribution of our simulated galaxies, $\tilde{\mu}_{B/T-tng50} = 0.09$, is even lower than the median value of the observed sample of Peebles (2020b), $\tilde{\mu}_{B/T-obs} = 0.16$. However, our selection criteria explicitly select highly triaxial galaxies, which can bias our sample to galaxies with lower photometric bulge luminosities. To provide a quantitatively meaningful comparison with observations, similar selection criteria for both the simulated and observational samples, as well as a larger observational sample would be needed. It is worth noting the lack of pure discs with a nuclear cluster (like, e.g. M101) in our sample of simulated late-type galaxies. Although the connection between dynamical and surface brightness decompositions is not straightforward (see Abadi et al. 2003), the point highlighted by Peebles (2020b) persists: bulgeless galaxies with very cold discs are not yet easy to achieve with the current set-up in state-of-the-art cosmological simulations. Peebles (2020b) proposes a second order deviation from gaussianity to the density fluctuations in the cosmological model to address this problem. However, according to the review by Lagos (2018) and the aforementioned work by Bois et al. (2010), there is still room to improve the dynamical and mass resolution, as well as the simplistic models of the interstellar medium of our current simulations.

7.1 Mergers and the *ex situ* fraction of stars in the bulge

The mergers of galaxy pairs with comparable sizes are long known to behave in an inelastic fashion and produce remnants resembling elliptical galaxies (Toomre 1977; Barnes 1988; Hernquist 1992, 1993). Whilst the merger scenario seems satisfactory for the formation of high-Sérsic bulges in galaxies with close to 1:1 mergers, it must be re-examined when talking about MW/M31-like galaxies or $L_\star$ galaxies, in light of the results of this work (see also Bell et al. 2017). Only mergers that reach the galactic center and contribute to the *ex situ* component of bulges seem to produce a noticeable effect on the shape of the final surface brightness profile of our galaxies. We confirm in this work the dominance of a single satellite (or a low number of them) in the *ex situ* component of bulges (see Section 4). This then disfavours the scenario of bulge formation via the accretion of many low mass satellites. These considerations do not ignore the importance of mergers in the formation and evolution of bulges, but seek only to discuss and reconsider the correlation of the number and kind of mergers with the formation of high-Sérsic bulges. Indeed, high-Sérsic bulges have more commonly higher fractions of *ex situ* stars than low-Sérsic bulges, as can be seen in the top panel of Fig. 7.

Finally, mergers still explain a large fraction of the stars formed in starburst events that end-up in bulges and may be responsible, in some cases, for triggering bar formation. This may, in turn, explain the formation of another large fraction of the stars that contribute to the formation of photometric bulges.

7.2 Low-Sérsic bulge formation due to bars and prevention of bar formation due to concentrated bulges

We showed in Section 6 that low-Sérsic bulges exhibit a higher fraction of bars at all redshifts. This can be interpreted as a causality. Bars grow, basically, due to transfer of angular momentum and are known drivers of photometric bulge growth, via two channels: (i) bars can contribute to photometric bulge growth via the inward pull of gas due to torques that later form stars in the bar itself, near the centre of the galaxy or in nuclear rings, as is predicted from simulations (Sanders & Huntley 1976; Athanassoula 1992; Kim et al. 2012) and confirmed with observations (Phillips 1996; Sakamoto et al. 1999; Fraser-McKelvie et al. 2020; Wang et al. 2020) and (ii) bringing stars already formed to inner regions, after reshaping their orbits. Stellar particles captured in resonances can lose orbital angular momentum due to the bar and spiral arms, and suffer a reshaping of their orbits that make them populate the bulge region (Sellwood & Binney 2002; Minchev & Famaey 2010). Another mechanism where stars are driven to the central regions can be explained by the invariant manifolds (Romero-Gómez et al. 2006; Athanassoula et al. 2009). These act as channels in the ends of bars where stars can be brought from outside co-rotation to the inner regions.

In this line of reasoning, bars would contribute statistically more to the formation of photometric bulges with lower Sérsic indices. Recent observational results from the TIMER survey (Bittner et al. 2020; Gadotti et al. 2020) support this scenario, as it was shown that nearby barred galaxies lead to the formation of inner discs with profiles close to exponential. However, the excess of bars in galaxies with low Sérsic indices can also be a consequence of concentrated bulges preventing the formation of bars. The notion of a strong concentration of mass in the central region of galaxies preventing the disc to become unstable was already presented by Toomre (1981) using linear perturbation theory. It was argued that the presence of a strong mass concentration could stop the feedback during the 'swing amplifier and feedback loop' process (see also chapter 6.3 from Binney & Tremaine 2008). More recently, Saha & Elmegreen (2018) and Kataria & Das (2018) used isolated *N*-body simulations, and showed that cold discs prevent the formation of a bar in the presence of highly concentrated bulges. Naturally, both the photometric bulge growth via star formation mechanisms associated with bars and the prevention of bar formation, or its strengthening due to a concentrated bulge, can be concomitant processes in a single galaxy or act with different strengths in different galaxies. This way, both processes are complementary to produce the trend shown in Fig. 14. To quantify to what degree these two combined processes lead to different bar fractions in high- and low-Sérsic photometric bulges, we would need a higher temporal resolution to follow the orbits of individual stars in galaxies and track their formation sites more accurately, in addition to having a larger number of high-mass resolution simulated galaxies to find a statistically meaningful sample of them with early central mass concentrations.

A third, methodological, fact that could contribute to the difference in the bar fractions in high- and low-Sérsic photometric bulges relies on the way we are measuring Sersic indices, which are obtained from a two-component photometric decomposition. As mentioned in Section 2.2.1, although the excess of light coming from bars is extracted when it is evident from the SBPs, some contamination that is absorbed by either of the two components remains. Short, weak bars, would contaminate more the Sérsic component whereas long bars would add more contamination to the disc component. Adding a third component to model the bar may yield different results, at the expense of more free parameters and uncertainties in the fitting procedure. In any case, it is beyond of the scope of this paper to compare both procedures.

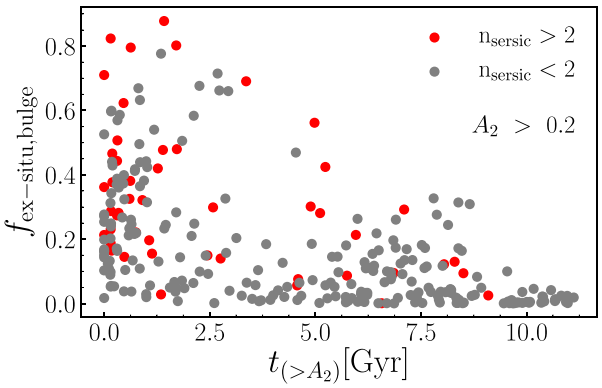

Figure 16. Fraction of *ex situ* stellar particles in bulges of simulated TNG50 MW/M31-like galaxies as a function of the time during which galaxies experienced a bar feature with $A_2 > 0.2$. Strong bars develop only in galaxies with *ex situ* fractions $f_{acc,bulge} \lesssim 0.2$.

An interesting trend also found in Section 6 was that of the duration of the bar feature above a given threshold with Sérsic index, B/T and the *ex situ* bulge fraction. Although there is no clear correlation between these properties, there is a group of galaxies that develop strong bars, have low *ex situ* bulge fractions and present mainly low Sérsic indices (see Fig. 15). These simulated galaxies develop in some cases large massive bulges none the less. The lack of large fractions of *ex situ* stars, the presence of a strong bar during most of their existence, and the development of large bulges in some cases, suggest the possibility that many of those photometric bulges were formed by star formation mechanisms driven by the bar. This is in line with the results shown in Fragkoudi et al. (2020), who found, using the Auriga simulations, that bars are more likely to form in galaxies which have low fraction of *ex situ* stars in their bulges. They furthermore split their barred sample into galaxies with and without boxy/peanut bulges, and showed that those that have a boxy/peanut bulge will have the lowest fraction of *ex situ* stars (see Fig. 14 of their article). In Fig. 16, we show the fraction of *ex situ* stars in the bulge, as defined in Section 4 as a function of duration of the bar, with a bar strength $A_2 > 0.2$. Clearly, strong bars mainly develop and prevail in the simulated galaxies with low to moderate *ex situ* fractions. This could indicate that either strong bars do not form if bulges already have accreted a large quantity of stars in a merger, as discussed earlier, or that the enhanced star formation produced by strong bars driving gas to the central regions increases the *in situ* bulge fraction. A group of galaxies show a relatively high *ex situ* fraction ($f_{ex\,situ} > 0.2$) and a strong bar duration $t_{>A_2} > 3$Gyr. These systems, where both scenarios combine can be classified as composite.

8 SUMMARY AND CONCLUSIONS

In this work, we have studied the origin of different types of bulges formed in a sample of MW/M31-like galaxies drawn from the state-of-the-art hydrodynamical cosmological simulation TNG50. Bulges are parametrized in terms of their Sérsic index and B/T ratios, which are derived from two-component photometric decompositions of their surface brightness profiles in the *V* band. In general, there is no trivial correlation between the concentration of the Sérsic profile that characterizes photometric bulges in simulated MW/M31-like galaxies and the aspects explored in this work, namely, the environment

where galaxies lie, the total number of mergers, the properties of the significant mergers they experience, and the presence of a bar. Instead, it is a combination of processes that contribute to form a bulge with a higher or lower Sérsic index in a MW/M31-like galaxy. The presence of strong bars and the occurrence of late mergers play the more significant role in shaping the inner regions of the surface brightness profiles, whereas bars are shown to be a fundamental driver of bulge mass growth in all types of bulges.

Our specific findings and conclusions are summarized and listed below:

(i) We found that, of our 287 MW/M31-like galaxies selected using the criteria defined in Section 2.2, 17.1 per cent have Sérsic index $n > 2$ (Fig. 3).

(ii) The Sérsic index of MW/M31-like galaxies in TNG50 are not affected by the environment. Two different methods, one considering the number of neighbours inside a fixed sphere of 738.2 kpc radius and the other that takes into account the overdensity of galaxies up to the k*th* neighbour, yield no measureable dependence on environment at $z = 0$. B/T ratios show a mild increase towards higher overdensities of galaxies (Fig. 6).

(iii) Galaxies with high-Sérsic index bulges show, on average, a higher fraction of *ex situ* stellar particles in the kinematically selected bulge than galaxies with low-Sérsic index bulges, by 19 percentage points (Fig. 7).

(iv) Mergers are ubiquitous in most simulated galaxies. The number and total mass accreted via mergers are not correlated with the level of concentration of bulges reflected by their Sérsic index (Fig. 10). The last considerable merger ($m_{\rm sat}/m_{\rm host} > 0.1$) occurs on average at later times in simulated galaxies with high-Sérsic index (Fig. 11), although a large number of them with low-Sérsic index also suffer a late massive merger.

(v) Bulge stellar particles in our sample of MW/M31-like galaxies, selected by means of kinematic considerations, are mostly formed *in situ*, as shown by previous works (Fig. 8). Also confirming previous results, a single satellite is commonly responsible for building 50 per cent of the *ex situ* component of bulges and a low number of satellites is enough to account for 90 per cent (Fig. 9).

(vi) The bar fraction in our sample of simulated MW/M31-like galaxies shows a reasonable agreement with the bar fraction measured at $z = 0$ and do not decrease towards higher redshifts, as observational estimates show for different samples of galaxies (Fig. 13). Simulated galaxies with high-Sérsic index bulges consistently show a lower bar fraction than those with low-Sérsic index bulges at all redshifts, pointing to a strong influence of bars in the formation of low-Sérsic bulges and the effect of concentrated bulges in preventing bar formation. Simulated galaxies with higher B/T ratios present a higher fraction of bars at all redshifts, indicating that bars are a prominent channel of photometric bulge growth in our sample of simulated galaxies (Fig. 14).

Upcoming theoretical attempts to describe and understand the subtleties of the formation of different types of galactic bulges in galaxies like our own and M31, in a cosmological context, should pursue the use of simulations with a challenging combination of characteristics: high dynamical and mass resolution, to ensure a realistic dynamical behaviour in central regions of simulated galaxies; large cosmological volumes, to capture the observed diversity of bulges, and more realistic ISM models.

ACKNOWLEDGEMENTS

We thank the reviewer, Isabel Pérez, for her insightful comments. I.G. acknowledges financial support from CONICYT Programa de Astronomía, Fondo ALMA-CONICYT 2017 31170048, *Consejo Nacional de Investigaciones Científicas y Técnicas* (CONICET, PIP-0387), *Agencia Nacional de Promoción de la Investigación, el Desarrollo Tecnológico y la Innovación* (Agencia I+D + i, PICT-2018-03743), and Universidad Nacional de La Plata (G11-150), Argentina. AM acknowledges support from FONDECYT Regular 1212046. FAG acknowledges support from FONDECYT Regular 1211370. IG, AM, and FAG acknowledge funding from the Max Planck Society through a 'Partner Group' grant. DN acknowledges funding from the Deutsche Forschungsgemeinschaft (DFG) through an Emmy Noether Research Group (grant number NE 2441/1-1). AP acknowledges support by the Deutsche Forschungsgemeinschaft (DFG, German Research Foundation) – Project-ID 138713538 – SFB 881 ('The Milky Way System', subproject A01). RG acknowledges financial support from the Spanish Ministry of Science and Innovation (MICINN) through the Spanish State Research Agency, under the Severo Ochoa Program 2020-2023 (CEX2019-000920-S). FM acknowledges support through the Program 'Rita Levi Montalcini' of the Italian MUR. The primary TNG simulations were carried out with compute time granted by the Gauss Centre for Supercomputing (GCS) under Large-Scale Projects GCS-ILLU and GCS-DWAR on the GCS share of the supercomputer Hazel Hen at the High Performance Computing Center Stuttgart (HLRS). The public package `PY-SPHVIEWER` (Benitez-Llambay 2015) was used to produce Fig. 1 of this paper.

DATA AVAILABILITY

The data used in this work is accesible via the IllustrisTNG public data base.[2] The Data from the Auriga simulations used for comparison is available upon reasonable request.

REFERENCES

Abadi M. G., Navarro J. F., Steinmetz M., Eke V. R., 2003, ApJ, 591, 499
Andredakis Y. C., Peletier R. F., Balcells M., 1995, MNRAS, 275, 874
Athanassoula E., 1992, MNRAS, 259, 345
Athanassoula E., 2005, MNRAS, 358, 1477
Athanassoula E., Romero-Gómez M., Bosma A., Masdemont J. J., 2009, MNRAS, 400, 1706
Athanassoula E., Machado R. E. G., Rodionov S. A., 2013, MNRAS, 429, 1949
Barnes J. E., 1988, ApJ, 331, 699
Bell E. F., Monachesi A., Harmsen B., de Jong R. S., Bailin J., Radburn-Smith D. J., D'Souza R., Holwerda B. W., 2017, ApJ, 837, L8
Benitez-Llambay A., 2015, py-sphviewer: Py-SPHViewer v1.0.0
Binney J., Tremaine S., 2008, Galactic Dynamics: Second Edition. Princeton University Press, Princeton
Bittner A. et al., 2020, A&A, 643, A65
Blaña Díaz M., Wegg C., Gerhard O., Erwin P., Portail M., Opitsch M., Saglia R., Bender R., 2017, MNRAS, 466, 4279
Blaña Díaz M. et al., 2018, MNRAS, 481, 3210
Bland-Hawthorn J., Gerhard O., 2016, ARA&A, 54, 529
Blanton M. R., Moustakas J., 2009, ARA&A, 47, 159
Blázquez-Calero G. et al., 2020, MNRAS, 491, 1800
Boardman N. et al., 2020, MNRAS, 498, 4943
Bois M. et al., 2010, MNRAS, 406, 2405
Brooks A., Christensen C., 2016, in Laurikainen E., Peletier R., Gadotti D., eds, Galactic Bulges, Astrophysics and Space Science Library, Vol. 418. Springer International Publishing, Switzerland, p. 317
Bruzual G., Charlot S., 2003, MNRAS, 344, 1000

[2] https://www.tng-project.org/data

Buck T., Ness M. K., Macciò A. V., Obreja A., Dutton A. A., 2018, ApJ, 861, 88
Ceverino D., Dekel A., Bournaud F., 2010, MNRAS, 404, 2151
Croton D. J. et al., 2006, MNRAS, 365, 11
de Vaucouleurs G., 1948, Ann. Astrophys., 11, 247
Dekel A., Sari R., Ceverino D., 2009, ApJ, 703, 785
Du M., Ho L. C., Debattista V. P., Pillepich A., Nelson D., Zhao D., Hernquist L., 2020, ApJ, 895, 139
Du M., Ho L. C., Debattista V. P., Pillepich A., Nelson D., Hernquist L., Weinberger R., 2021, ApJ, 919, 135
Dubois Y. et al., 2020, A&A, 651, A109
Elmegreen B. G., 1995, MNRAS, 275, 944
Elmegreen B. G., Elmegreen D. M., Fernandez M. X., Lemonias J. J., 2009, ApJ, 692, 12
Engler C. et al., 2021, MNRAS, 507, 4211
Erwin P. et al., 2015, MNRAS, 446, 4039
Fisher D. B., Drory N., 2008, AJ, 136, 773
Fisher D. B., Drory N., 2010, ApJ, 716, 942
Fisher D. B., Drory N., 2011, ApJ, 733, L47
Fisher D. B., Drory N., 2016, in Laurikainen E., Peletier R., Gadotti D., eds, Galactic Bulges, Astrophysics and Space Science Library, Vol. 418. Springer International Publishing, Switzerland, p. 41
Flynn C., Holmberg J., Portinari L., Fuchs B., Jahreiß H., 2006, MNRAS, 372, 1149
Fragkoudi F. et al., 2020, MNRAS, 494, 5936
Fraser-McKelvie A. et al., 2020, MNRAS, 495, 4158
Freeman K. C., 1970, ApJ, 160, 811
Gadotti D. A., 2009, MNRAS, 393, 1531
Gadotti D. A., 2012, preprint (arXiv:1208.2295)
Gadotti D. A. et al., 2020, A&A, 643, A14
Gao H., Ho L. C., Barth A. J., Li Z.-Y., 2018, ApJ, 862, 100
Gargiulo I. D., Cora S. A., Vega-Martínez C. A., Gonzalez O. A., Zoccali M., González R., Ruiz A. N., Padilla N. D., 2017, MNRAS, 472, 4133
Gargiulo I. D. et al., 2019, MNRAS, 489, 5742
Genel S. et al., 2014, MNRAS, 445, 175
Gómez F. A., White S. D. M., Grand R. J. J., Marinacci F., Springel V., Pakmor R., 2017, MNRAS, 465, 3446
Graham A. W., Driver S. P., 2005, Publ. Astron. Soc. Aust., 22, 118
Grand R. J. J. et al., 2017, MNRAS, 467, 179 (G2017)
Grand R. J. J., Springel V., Gómez F. A., Marinacci F., Pakmor R., Campbell D. J. R., Jenkins A., 2016, MNRAS, 459, 199
Grand R. J. J. et al., 2021, MNRAS, 507, 4953
Guedes J., Mayer L., Carollo M., Madau P., 2013, ApJ, 772, 36
Hernquist L., 1992, ApJ, 400, 460
Hernquist L., 1993, ApJ, 409, 548
Hopkins P. F., Cox T. J., Younger J. D., Hernquist L., 2009, ApJ, 691, 1168
Kataria S. K., Das M., 2018, MNRAS, 475, 1653
Kent S. M., 1985, ApJS, 59, 115
Kim W.-T., Seo W.-Y., Stone J. M., Yoon D., Teuben P. J., 2012, ApJ, 747, 60
Koekemoer A. M. et al., 2011, ApJS, 197, 36
Kormendy J., 1977, ApJ, 218, 333
Kormendy J., Kennicutt Robert C. J., 2004, Ann. Rev. Astron. Astrophys., 42, 603
Kunder A. et al., 2016, ApJ, 821, L25
Kunder A. et al., 2020, AJ, 159, 270
Lagos C. d. P., 2018, preprint (arXiv:1810.13074)
Laurikainen E., Salo H., Buta R., 2005, MNRAS, 362, 1319
Licquia T. C., Newman J. A., 2015, ApJ, 806, 96
Lintott C. J. et al., 2008, MNRAS, 389, 1179
Lovell M. R., Frenk C. S., Eke V. R., Jenkins A., Gao L., Theuns T., 2014, MNRAS, 439, 300
Lovell M. R. et al., 2018, MNRAS, 481, 1950
Luo Y. et al., 2020, MNRAS, 493, 1686
Marchesini D., Stefanon M., Brammer G. B., Whitaker K. E., 2012, ApJ, 748, 126
Marinacci F. et al., 2018, MNRAS, 480, 5113
Martig M., Bournaud F., Croton D. J., Dekel A., Teyssier R., 2012, ApJ, 756, 26
Melvin T. et al., 2014, MNRAS, 438, 2882
Méndez-Abreu J., Debattista V. P., Corsini E. M., Aguerri J. A. L., 2014, A&A, 572, A25
Menéndez-Delmestre K., Sheth K., Schinnerer E., Jarrett T. H., Scoville N. Z., 2007, ApJ, 657, 790
Minchev I., Famaey B., 2010, ApJ, 722, 112
Monachesi A., Bell E. F., Radburn-Smith D. J., Bailin J., de Jong R. S., Holwerda B., Streich D., Silverstein G., 2016, MNRAS, 457, 1419
Monachesi A. et al., 2019, MNRAS, 485, 2589
Mould J., 2013, Publ. Astron. Soc. Aust., 30, e027
Naiman J. P. et al., 2018, MNRAS, 477, 1206
Nelson D. et al., 2015, Astron. Comput., 13, 12
Nelson D. et al., 2018, MNRAS, 475, 624
Nelson D. et al., 2019a, Comput. Astrophys. Cosmol., 6, 2
Nelson D. et al., 2019b, MNRAS, 490, 3234
Nelson E. J. et al., 2021, MNRAS, 508, 219
Okamoto T., 2013, MNRAS, 428, 718
Pakmor R., Marinacci F., Springel V., 2014, ApJ, 783, L20
Peebles P. J. E., 2020a, Cosmology's Century: An Inside History of our Modern Understanding of the Universe. Princeton University Press, Princeton
Peebles P. J. E., 2020b, MNRAS, 498, 4386
Peebles P. J. E., Nusser A., 2010, Nature, 465, 565
Perez J., Valenzuela O., Tissera P. B., Michel-Dansac L., 2013, MNRAS, 436, 259
Phillips A. C., 1996, in Buta R., Crocker D. A., Elmegreen B. G., eds, ASP Conf. Ser. Vol. 91, IAU Colloq. 157: Barred Galaxies. Astron. Soc. Pac., San Francisco, p. 44
Pillepich A., Madau P., Mayer L., 2015, ApJ, 799, 184
Pillepich A. et al., 2018a, MNRAS, 473, 4077
Pillepich A. et al., 2018b, MNRAS, 475, 648
Pillepich A. et al., 2019, MNRAS, 490, 3196
Pillepich A., Nelson D., Truong N., Weinberger R., Martin-Navarro I., Springel V., Faber S. M., Hernquist L., 2021, MNRAS, 508, 4667
Pulsoni C., Gerhard O., Arnaboldi M., Pillepich A., Nelson D., Hernquist L., Springel V., 2020, A&A, 641, A60
Rodriguez-Gomez V. et al., 2015, MNRAS, 449, 49
Rodriguez-Gomez V. et al., 2016, MNRAS, 458, 2371
Romero-Gómez M., Masdemont J. J., Athanassoula E., García-Gómez C., 2006, A&A, 453, 39
Rosas-Guevara Y. et al., 2021, preprint (arXiv:2110.04537)
Saglia R. P. et al., 2010, A&A, 509, A61
Saha K., Elmegreen B., 2018, ApJ, 858, 24
Sakamoto K., Okumura S. K., Ishizuki S., Scoville N. Z., 1999, ApJ, 525, 691
Sanders R. H., Huntley J. M., 1976, ApJ, 209, 53
Scoville N. et al., 2007, ApJS, 172, 1
Sellwood J. A., Binney J. J., 2002, MNRAS, 336, 785
Sérsic J. L., 1963, BAAA, 6, 41
Sérsic J. L., 1968, Atlas de Galaxias Australes. Observatorio Astronomico, Universidad Nacional de Cordoba, Córdoba, Argentina
Shen J., Rich R. M., Kormendy J., Howard C. D., De Propris R., Kunder A., 2010, ApJ, 720, L72
Sheth K. et al., 2008, ApJ, 675, 1141
Sick J., Courteau S., Cuillandre J.-C., Dalcanton J., de Jong R., McDonald M., Simard D., Tully R. B., 2015, in Cappellari M., Courteau S., eds, Galaxy Masses as Constraints of Formation Models, Proc. IAU Symp., Vol. 311. p. 82
Sijacki D., Springel V., Di Matteo T., Hernquist L., 2007, MNRAS, 380, 877
Simmons B. D. et al., 2014, MNRAS, 445, 3466
Sparre M., Springel V., 2016, MNRAS, 462, 2418
Springel V., 2010, MNRAS, 401, 791
Springel V., Hernquist L., 2003, MNRAS, 339, 289
Springel V. et al., 2018, MNRAS, 475, 676
Tacchella S. et al., 2019, MNRAS, 487, 5416
Tamm A., Tempel E., Tenjes P., Tihhonova O., Tuvikene T., 2012, A&A, 546, A4

Tissera P. B., White S. D. M., Scannapieco C., 2012, MNRAS, 420, 255
Tissera P. B., Beers T. C., Carollo D., Scannapieco C., 2014, MNRAS, 439, 3128
Tissera P. B., Machado R. E. G., Carollo D., Minniti D., Beers T. C., Zoccali M., Meza A., 2018, MNRAS, 473, 1656
Toomre A., 1977, in Tinsley B. M., Larson Richard B., Gehret D. C., eds, Evolution of Galaxies and Stellar Populations. p. 401
Toomre A., 1981, in Fall S. M., Lynden-Bell D., eds, Structure and Evolution of Normal Galaxies. Cambridge University Press, Cambridge, p. 111
Vogelsberger M. et al., 2014a, MNRAS, 444, 1518
Vogelsberger M. et al., 2014b, Nature, 509, 177
Wang J., Athanassoula E., Yu S.-Y., Wolf C., Shao L., Gao H., Randriamampand ry T. H., 2020, ApJ, 893, 19
Weinberger R. et al., 2017, MNRAS, 465, 3291
Weinzirl T., Jogee S., Khochfar S., Burkert A., Kormendy J., 2009, ApJ, 696, 411

APPENDIX A: RESOLUTION CONVERGENCE

In this appendix, we conduct an analysis of the resolution convergence of the SBPs used to obtain the parameters of the two-component fits described in Section 2.2.1. For that purpose, we compare the values of surface brightness in radial bins of the SBPs, in the sample of MW/M31-like galaxies in TNG50-1 (labelled as TNG50 throughout this article) with those of galaxies residing in the analogous DM haloes in the sibling simulations of lower resolution TNG50-2 and TNG50-3 (see the illustrisTNG project webpage for a complete description of the simulations). We exclude from our analysis the TNG50-4 simulation, which has a resolution level that is a factor 512 lower, and a softening length a factor of 8 times larger. A thorough resolution convergence analysis of the TNG50 simulation in quantities like the disc sizes, disc scale heights, and kinematic measures can be found in Pillepich et al. (2019).

In order to compare the SBPs on a galaxy–galaxy basis me must find the analogue galaxies of our original sample in TNG50-1, in the lower resolution realizations. For that purpose, galaxies were matched between simulations using the data base produced in Lovell et al. (in preparation) with the matching algorithm described in Lovell et al. (2014, 2018). In this implementation, analogue objects are identified using the initial conditions. DM haloes that originated from the same Lagrangian patch in the initial conditions are considered analogues accross simulations. However, a perfect match does not always occur. DM haloes are tagged with a score, based on a quality-of-match statistic that indicates the certainty of the match. Scores close to 1 indicate a perfect match, while scores lower than 0.5 indicate that there is no match. Almost all galaxies of our sample of 287 MW/M31-like galaxies in TNG50-1 have a match in TNG50-2 and TNG50-3, with a score higher than 0.8. Only three of them have no counterpart in the lower resolution runs.

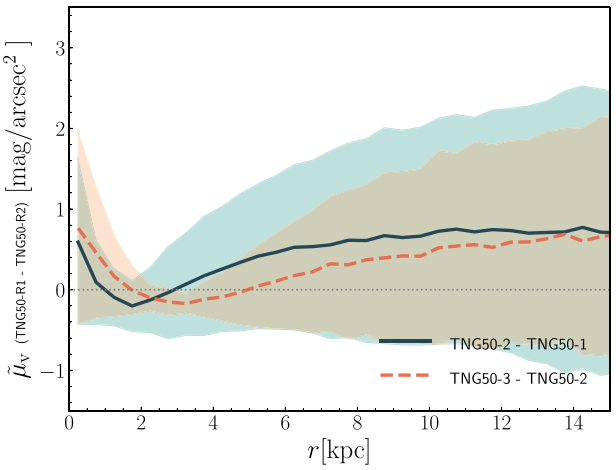

Figure A1. Binned median values of the difference of surface brightness as a function of radius for our sample of simulated galaxies in different resolution hierarchies. The solid dark green line shows the median of the difference between analogues in the TNG50-2 simulation and galaxies in our sample in TNG50-1 and the green filled region shows the corresponding interquartile ranges. The dashed orange line and filled orange region shows the same, but for TNG50-3 and TNG50-2. A dotted grey line indicates the zero difference value as visual aid. The SBPs in central regions of MW/M31-like galaxies are not fully converged in the highest resolution run in TNG50.

Fig. A1 shows the median difference of surface brightness in each radial bin of the SBPs between galaxies in TNG50-1 and their analogue galaxies in TNG50-2 and between these analogues in TNG50-2 and TNG50-3. We can see that in the central region, the median difference is positive in both cases, meaning that surface brightness profiles in TNG50-1 have a statistical excess in surface brightness there with respect to TNG50-2. Accordingly, TNG50-2 analogues show an excess of surface brightness in central regions with respect to analogues in TNG50-3. The difference between TNG50-2 and TNG50-3 is close to 0.8 mag arcsec^{-2}, while between TNG50-1 and TNG50-2 the median difference is close to 0.6 mag arcsec^{-2}. At radii in the range [1,3] kpc, the median difference becomes slightly negative between TNG50-2 and TNG50-1, probably due to the presence of brighter bars in TNG50-1. The median difference between TNG50-3 and TNG50-2 analogues becomes negative in the range [2,5] kpc. Moving to the outer regions, the median difference in the SBP becomes more substantial, as the surface brightnesses of discs diminishes.

This paper has been typeset from a TEX/LATEX file prepared by the author.